Investigating the Milky Way's Magnetism: A statistical analysis of the structural scales in polarized radio observations of our Galaxy

by

Robert Adrian Stutz

B.Sc. (Hons.), The University of British Columbia, 2009

A THESIS SUBMITTED IN PARTIAL FULFILLMENT OF
THE REQUIREMENTS FOR THE DEGREE OF

MASTER OF SCIENCE

in

The College of Graduate Studies

(Interdisciplinary Studies)

THE UNIVERSITY OF BRITISH COLUMBIA

(Okanagan)

September 2011

Abstract

Angular power spectra are calculated and presented for the entirety of the Canadian Galactic Plane Survey polarization dataset at 1.4 GHz. The data analyzed is a combination of data from the 100-m Effelsberg Telescope, the 26-m telescope at the Dominion Radio Astrophysical Observatory, and the Synthesis Telescope at the Dominion Radio Astrophysical Observatory, allowing all relevant scales to be sampled down to arcminute resolution. Calculated angular power spectra cover multipoles from $\ell \approx 60$ to $\ell \approx 10^4$, and display at least three distinct regions within this range. A power-law region at low multipoles, a flattening region at intermediate multipoles, and a taper region at high multipoles necessitate a model fitting routine for analysis. Power-law indices are found to have a mode of 2.3, similar to other results, though slightly steeper. An increasing trend in power-law index is found with increasing latitude. A transition from small-scale to large-scale structure is evident at b = $10°$. Flattening of the power spectra is also investigated and found to be likely due to background point sources, though this remains inconclusive.

Table of Contents

List of Figures

Acknowledgements

I would like to extend my thanks to my supervisor, Professor Erik Rosolowsky, for his continued support and helpful advice throughout the investigation and writing of this thesis. I would also like to thank Dr. Tom Landecker for providing both the original research direction as well as continual advice and invaluable knowledge of the subject matter. Dr. Roland Kothes and Dr. Marijke Haverkorn also deserve considerable gratitude for their helpful input and illuminating discussions. The staff at the Dominion Radio Astrophysical Observatory in general were exceedingly helpful and supportive, for which I am very grateful.

Finally, I must thank my partner Natasha Drew for continuing to support and encourage me in my attempts at completing this thesis, and for bearing the brunt of the fallout associated with this endeavour.

Chapter 1

Introduction

1.1 Polarization Studies and Angular Power Spectra

The magnetic field of our Milky Way Galaxy is commonly divided into two distinct but equally important components: the large-scale field on scales of the spiral arms of the Galaxy, and the small-scale field on scales of stellar activity. Both components are locked into the interstellar medium plasma by their interactions with charged particles. The large-scale field has a magnetic field strength of $\sim 2\mu G$ at the solar radius, and appear to follow the spiral arms of increased matter density within the Galaxy, staying parallel to the plane of the galactic disk. The magnetic field strength increases to $\sim 10\mu G$ at the galactic center [Landecker, 2011]. The magnetic field direction of this large-scale field undergoes a reversal inside the solar radius, and other field reversals have been proposed but remain a subject of debate [Beck, 2009]. This large-scale field is not sampled directly by the observations presented in this thesis, but it remains an important topic in galactic evolution.

The small-scale component of the magnetic field is a diffuse quasi-random field, exhibiting none of the overlying structure associated with the large-scale field. Individual structures in the diffuse magnetic field reach scales on the order of tens of parsecs. Nonetheless, the small-scale component has a similar strength to that of the large-scale field, reaching $\sim 3\mu G$ at the solar radius [Landecker, 2011]. As the magnetic field is locked into the interstellar medium, any perturbations of this medium due stellar events also affect the magnetic field; events like supernovae directly alter this small-scale diffuse magnetic field. The turbulence of the diffuse field is greater in the arm regions compared to the interarm regions due to the increased stellar activity within the Galaxy's spiral arms. This component of the magnetic field is indirectly studied in this thesis by analysing the continuum emission associated with the magnetic field lines.

The continuum emission that is detected by radio telescopes when ob-

serving the plane of our Galaxy is due to the spiraling of cosmic rays around the magnetic field lines of the Galaxy. These magnetic field lines may be part of the large regular component of the field or small-scale irregular components. Cosmic ray electrons are affected by this magnetic field and begin to spiral along the field lines, producing continuum synchrotron emission [Burke, 2010]. This emission may be partially polarized, and as it propagates on its way to Earth, it is affected and altered by the warm magnetized interstellar medium through which it passes. Observations of this emission by radio telescopes on Earth thus hold information both about the original emission mechanism and strength as well as the medium through which it travels. Unfortunately the study of radio polarization is complicated by the lack of correlation between radio polarization images and total intensity radio images. Faraday depolarization and other depolarization mechanisms alter the original emission to the point where it bears little resemblance to physical objects at the point of emission.

Increasing the understanding of polarization observations is essential for understanding evolutionary galactic dynamics and the prevalence of our Galaxy's cosmic magnetism. The magnetic field of our Galaxy is expected to have an impact on many of the processes within the Galaxy from individual star formation to the density waves in the Galaxy that produce its spiral arms. Increasing the understanding of the cosmic magnetism in our Galaxy will allow us to more completely describe the dynamical processes which shape its interstellar medium and the structures and objects in that interstellar medium which it influences.

Structures visible in polarized intensity are often entirely missing in total intensity maps of the same regions. Interpretation of polarization maps is further confounded by a lack of knowledge on the distance scales involved in depolarization effects. That is, it is often impossible to determine whether the modulation of polarized emission occurs at a significant distance from the point of emission, or whether it occurs at a much greater distance along the path of propagation through the warm interstellar medium. These factors compound to produce polarization images which not only appear completely different from total intensity images but are also hard to classify into individual objects. Distant emission may be modulated many times on its path to Earth, and it is nearly impossible to determine the foreground object responsible for the most significant effects [Landecker et al., 2010].

Polarization observations are subject to the same resolution constraints as their corresponding total intensity observations; thankfully, they also permit the use of synthesis radio telescopes to improve their resolution. The fundamental Rayleigh criterion states that the angular resolution of a tele-

scope is proportional to the observed wavelength and inversely proportional to the diameter of the telescope; a smaller angular resolutions allows a telescope to resolve smaller objects. As radio telescopes operate at the longest observable wavelengths they must compensate by increasing their dish sizes. Alternatively, aperture synthesis techniques allow pairs of radio telescopes to act as a single-dish telescope of a diameter equal to their separation. The use of synthesis telescopes to sample the smallest scales in radio observations has its own drawbacks, namely that large-scale structure is lost due to its inability to be sampled by the phyisically separated antenna of such a telescope. Large single-dish telescopes operating in the radio regime sample such large scales accurately, but cannot approach the size of synthesis arrays [Verschuur, 2007]. Only with a combination of single-dish and synthesis telescope observations can all scales of the galactic polarized emission be sampled accurately.

The analysis of polarized intensity data is often done in terms of the structural scales in the images. Angular power spectra, which convey the power present at specific angular scales, are used to determine the distribution of power in the observations. Since identification and taxonomy of individual objects in polarized intensity maps is difficult, such broad-approach statistical analyses allow us to describe the observed polarized medium without having to deal with classification issues. In previous studies the power spectra are generally given as a function of multipole ℓ, which is inversely proportional to angular scales in the observations. Specifically, $\ell \approx 180°/\theta$, where θ corresponds to the angular scales in the image in degrees. Further discussion will focus on both angular scales for simplicity and their corresponding multipoles for the sake of comparison with previous studies.

The radio continuum survey used in this thesis is detailed below in Section 1.2, and analyzed in Section 2. The results of the analysis are described in Section 3.1. The source of the observed radio emission - synchrotron emission - is discussed in Appendix A. Important polarization definitions and depolarization effects are outlined in Appendix B.

1.2 Canadian Galactic Plane Survey Polarization Maps

The polarization maps analyzed in this thesis are part of the Canadian Galactic Plane Survey (CGPS) datasets presented in Landecker et al. [2010]. This survey is an international collaboration led by Canadian researchers, with its principal aim being to fully map the total intensity and the polarized

intensity of the portion of the Milky Way galaxy visible in the northern hemisphere. Continuum polarized emission around 1420 MHz was measured for 1060 square degrees of the nothern Galactic plane down to a resolution of ~ 1 arcminute. The survey extends from a galactic longitude of l = 66° to l = 175° over the latitude range from b = −3° to b = 5°. The survey area is divided into six data maps, termed supermosaics, that each cover the entirety of the observed galactic latitudes and a range of galactic longitudes. In addition to the main survey a high-latitude extension up to b = 17.5° was observed from l = 101° to l = 116°.

The CGPS polarization survey is unique both in size and in the fact that the final dataset is a combination of observations from three seperate telescopes. Encompassing observations from ~ 1995 to ~ 2005, the data is a combination of observations from the Effelsberg 100-m Telescope, the Dominion Radio Astrophysical Observatory (DRAO) 26-m Telescope, and the DRAO Synthesis Telescope. The aim of this combination is to fully sample the polarized sky on all angular scales, especially the largest scales that are missed by other synthesis-only surveys.

A brief analysis of the polarization maps is also given in Landecker et al. [2010], with the most salient points discussed here. As seen throughout the literature of polarization studies, the polarized intensity sky and total intensity sky have few similarities. This is visually obvious in Figures 5 - 7 in Landecker et al. [2010], and is generally agreed to be due to Faraday rotation effects and depolarization. The polarization fraction throughout the survey is near 10%, significantly lower than the theoretical maximum of 70%, providing further evidence for the existence of a significant depolarization mechanism. The polarized sky also appears to have features on wildly varying scales. Large-scale polarization features are evident, and are assumed to be connected with the large-scale features of the galactic magnetic field itself, being roughly aligned with the spiral arms of the Galaxy. Small-scale variations appear more randomly distributed, and may reflect the irregular component of the magnetic field and the turbulence of the ionized gas. Power may be shifted from larger scales to smaller scales by depolarization effectively randomizing areas of the large-scale emission. Landecker et al. [2010] note that at the survey frequency of 1420 MHz the irregular component is obvious but does not dominate the larger regular component. As Faraday rotation increases at longer wavelengths, it is conceivable that a wavelength exists beyond which the regular component of the polarized emission is entirely obscured. This thesis concerns itself mainly with the distribution of power between the large-scale regular component of the emission (and thus magnetic field) and the small-scale irregular component.

1.2.1 Effelsberg Telescope Observations

Part of the CGPS polarization data is made up of observations from the 100-m Telescope near Effelsberg, Germany. The polarization dataset observed at the Effelsberg 100-m telecope are part of the results from the *Effelsberg Medium Latitude Survey*, which ran from 1994 to 2005 [Reich et al., 2004]. While various polarimeters were utilized during the survey, the telescope nominally observed at a central frequency of 1400 MHz with a bandwidth of 20 MHz. At this frequency the telescope's main beam is approximated by a Gaussian with a half-power-beam-width of 9.35', and the total system noise temperature is around 26 K. While the total intensity is noise-limited around 15 mK, the sensitivity in Stokes Q and U individually is as low as 8 mK. The receiving system is further discussed in Uyaniker et al. [1998], and any further parameters important for the CGPS data are outlined in Landecker et al. [2010].

1.2.2 26-m Telescope Observations

A second component of the full datasets presented in Landecker et al. [2010] is provided by the 26-m Telescope located at the DRAO. This telescope is actually a 25.6 m equatorially mounted, axially symmetric dish. At an observing frequency of 1.4 GHz this dish has a beamwidth of 36', significantly lower than the resolutions for the other two telescopes. However, the data are corrected for ground radiation, allowing the telescope to sample large angular scales. The system temperature of the dish is around 125 K, with a sensitivity of 12 mK in Stokes Q and U. The bandwidth of the polarization measurements around 1410 MHz is 12 MHz, for which range the polarimeter provides the normal power channels of RR, LL and the cross products RL and LR. Parameters of significance for the survey can be found in Landecker et al. [2010], with a full treatment of the receiving system presented in Wolleben et al. [2006].

1.2.3 The Synthesis Telescope at the DRAO

The third component of the finalized datasets presented in Landecker et al. [2010] is provided by the Synthesis Telescope at the DRAO. The data presented and analyzed in this thesis deals primarily with the combined polarization datasets, but some emphasis is also given to the synthesis data alone. For this reason a more thorough treatment of the synthesis telescope's parameters is given below. The present data were observed between 1995

April and 2004 March, so the given parameters are an average description of the telescope array and its characteristics over that period.

The synthesis telescope located at the DRAO consists of seven equatorially mounted parabolic antennas arrayed in an east-west configuration. An array of seven antennas gives only 21 instantaneous baselines, thus the east-west configuration was chosen to allow for Earth's rotation to vary the baseline vectors. Four of the antennas remain in a fixed position in the array, while three are moveable along a rail track running east to west. Having such movable elements in the array allows for intermediate baselines to be sampled. Five of the antennas have a diameter of 8.53m, the other two have a diameter of 9.14m. The configuration of the antennas as seen in Figure 1.1 has a baseline increment of $L = 4.286$m, approximately half the antenna diameters of 8.53m. Complete coverage of all baselines from $3L$ to $141L$ (plus $144L$) can be obtained with 12 different array configurations. The total time required for complete sampling of the entire aperture is then 12×12 hours [Landecker et al., 2000].

The minimum usable baseline corresponds to $3L \simeq 12.86$m due to mechanical interference considerations. This corresponds to a maximum size for sampled structures of ~ 40' at 1420 MHz. The largest baselines sampled by the synthesis telescope are $144L \simeq 617.1$m, giving a resolution of 58". [Landecker et al., 2000].

The difference in antenna diameters results in significantly different weightings of u-v samples, but a method of corrections has been devised by Willis [1999]. Antenna noise temperatures also vary from a maximum of 26.0 K for one antenna to a minimum of 17.8 K for another. The synthesis telescope had a total system temperature of 60 K for most of the survey, improving to 45 K in 2003. The telescope's sensitivity was consequently improved from 0.30 mJy beam^{-1} to 0.23 mJy beam^{-1}. The frequency coverage of the synthesis receiver bands is displayed in Figure 1.2. Continuum polarization measurements utilize bands A,B,C, and D of the receiver, each of width 7.5 MHz.

1.2.4 Combination of Synthesis and Single Dish Datasets

The CGPS dataset presented in Landecker et al. [2010] is unique in that it is the first extensive polarization survey that accurately samples information on all scales by combining synthesis and single-dish telescope data. The data from the DRAO Synthesis Telescope, the 100-m Effelsberg Telescope, and the DRAO 26-m Telescope are combined in an attempt to mitigate problems with the individual telescopes. The motivation and results of this
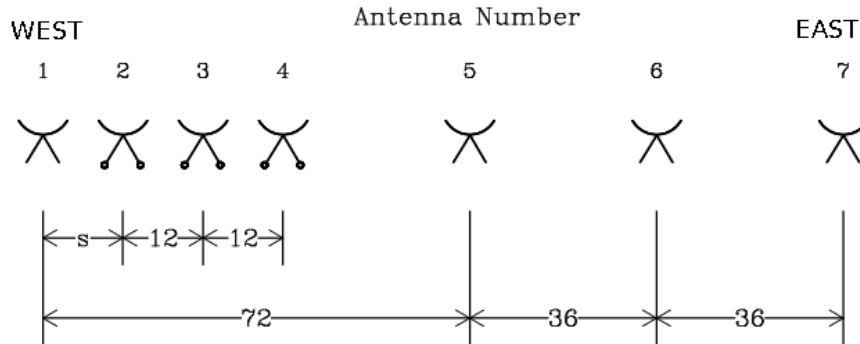
Figure 1.1: DRAO synthesis telescope configuration. Antenna separations given in units of $L = 4.286$m. The separation between antennas 1 and 2 can be modified from $3L$ to $14L$ by movement along the track.

combination are briefly outlined below, with full details available in Landecker et al. [2010].

The motivation for combining datasets arises from the issues that each telescope faces. While the Synthesis Telescope has an adequate maximum resolution corresponding to a multipole of $\ell \sim 7700$, it is limited to observing baselines longer than 12.86 m, the minimum phyical separation of antennas. This corresponds to an angular size of ~ 40', or a multipole of $\ell \sim 270$. Further complications arise as the ground radiation is detected as polarized emission in the sidelobes of both antennas when spaced so closely. This makes the 12.86 m baselines unusable for polarization imaging, so larger scales and extended structure remain unsampled by the Synthesis Telescope [Landecker et al., 2010].

The 100-m Effelsberg Telescope has an adequate resoluion of ~ 9.35' and can sample larger scales, but it is similarly limited by the data processing. A linear baseline is subtracted from each field in order to set the edges to zero, which effectively removes ground radiation. Unfortunately any real data at scales approaching the field sizes would also be removed by this process. The Effelsberg fields range in size from $5°$ to $16°$; any structures on the size scale of the field or larger will be lost. Taking the $5°$ fields as the limiting case, the Effelsberg Telescope nominally samples multipoles between $\ell \sim 40$ and $\ell \sim 1200$.

The data from the smaller 26-m Telescope has correct zero levels and does not require removal of the ground radiation, allowing the largest scales and smallest multipoles to be sampled. However, the resolution for the 26-m Telescope of ~ 36', corresponding to a multipole of $\ell \sim 300$, is significantly
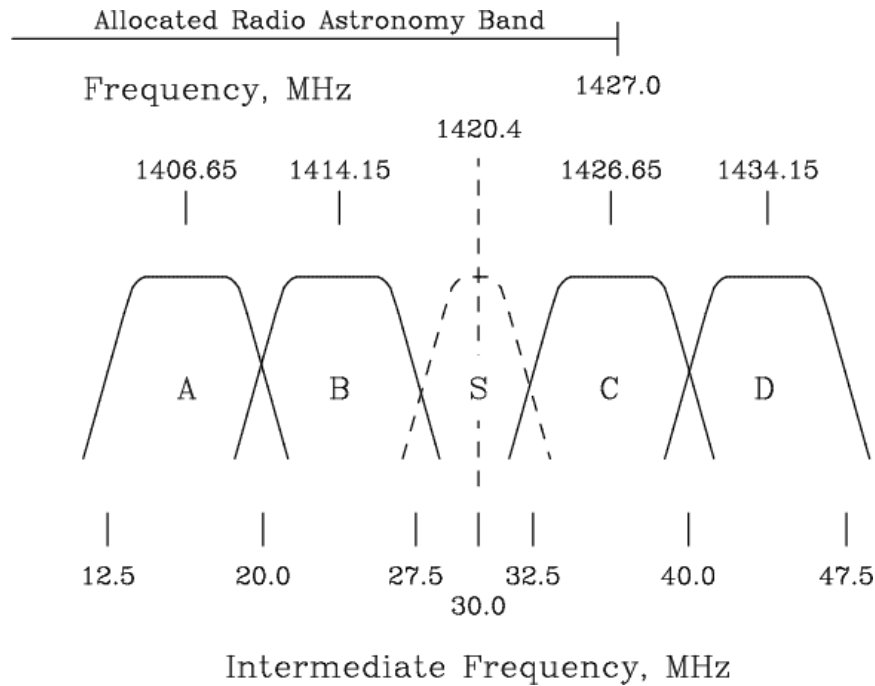
Figure 1.2: Arrangement of continuum and spectroscopy bands around 1420 MHz for the synthesis receiver. Hydrogen spectroscopy is done in the S band; continuum observations occur in bands A,B,C,D. Frequencies below the bands give the intermediate frequencies that the signals are converted to. Protected bands allocated to radio astronomy are also indicated.

worse than the other two telescopes. The separations between drift scans of the 26-m Telescope are also often too large to provide a fully sampled coverage of the survey; the sky sampling is only 41% of full Nyquist. The Effelsberg dataset is used to fill in the gaps in the 26-m data.

Comparisons of the datasets were undertaken to demonstrate the feasibility and accuracy of combining the data. A pixel-by-pixel comparison plot of the same sky region in the 26-m and 100-m datasets does not give a slope of exactly 1 as expected, nor does it pass through the origin. This systematic offset remains unexplained, but Landecker et al. [2010] nonetheless conclude that the two intensity scales are within $\sim 5\%$. A comparison of the Effelsberg and Synthesis datasets shows that at baselines below 15 m the power in the Effelsberg data exceeds that from the Synthesis Telescope. This is expected due to the inability of the Synthesis Telescope to sample these short baselines. Apart from this expected discrepancy the two
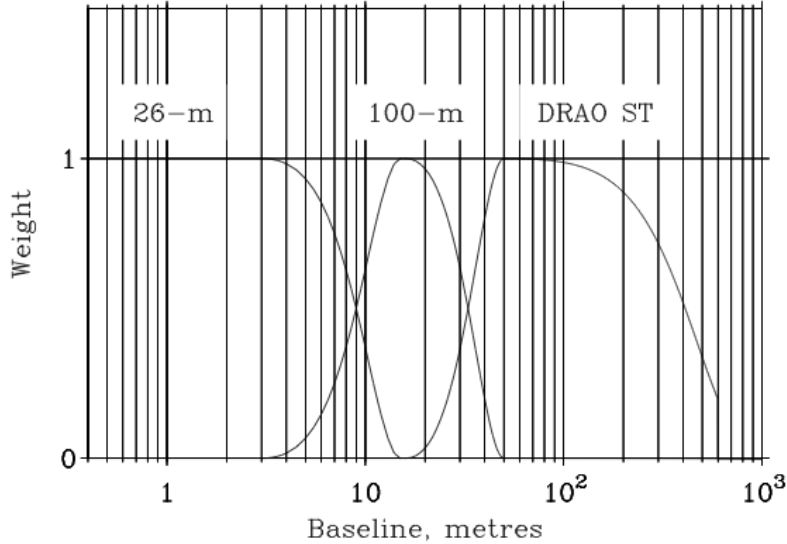
Figure 1.3: Fig. 3 from Landecker et al. [2010]. Weighting of the three datasets over the spatial coverage of the survey. Also shown is the apodization function applied to the Synthesis Telescope data at the longest baselines.

datasets are found to be within $\sim 10\%$.

A combination of the three datasets allows for the 26-m data to sample the largest structures, the Effelsberg data to fill in the gaps in the 26-m data, and the Synthesis telescope data to provide small-scale information with its superior resolution. A simplified approximation of the weighting given to each telescope dataset across the baselines of the survey is given in Figure 1.3 taken from Landecker et al. [2010]. A Gaussian apodization function is also applied at the longest baselines strictly in the Synthesis regime, in order to diminish the contributions of the sidelobes to the antenna beam. The applied Gaussian reaches 20% at the longest baseline of 617m.

The transitions between telescopes in Figure 1.3, where the weightings reach 0.5, occur at a baseline of 9m for the 26-m to 100-m transition, and a baseline of ~ 33m for the 100-m to Synthesis transition. The corresponding multipoles are $\ell \sim 110$ and $\ell \sim 400$ respectively. The extent of the apodization function means the Synthesis Telescope samples multipoles up to $\ell \sim 7700$, which is then also the upper limit of the combined dataset.

Chapter 2

Analysis and Results

2.1 Calculating Angular Power Spectra

To determine the distribution of power across the angular scales of the CGPS polarization data we calculate and analyze angular power spectra (APS) of the data. This calculation of APS can also be used for the single-dish maps. The method for calculating APS closely follows that of Haverkorn et al. [2003], though the analysis differs significantly due to slightly better resolution and the inclusion of larger scales in the CGPS data.

The map to be analyzed is Fourier transformed into the spatial frequency domain and then multiplied by its complex conjugate to calculate power:

$$PS_X(\ell) = \mathcal{F}(X) \times \mathcal{F}^*(X). \tag{2.1}$$

X may be any of the Stokes parameters Q, U, or PI for which polarization maps exist, though power spectra presented here are generally calculated for polarized intensity PI unless otherwise noted. Due to the nature of the Fourier transform, this is best accomplished by taking square maps or submaps from the supermosaics. The calculated PS_X is a two-dimensional representation of the power data, so it is averaged in radial bins to determine the one-dimensional power behaviour. The radial bins are taken outward from the center of the Fourier transformed image in one-pixel increments. The standard deviation within each ring is also calculated and is divided by the square root of the number of data points to give the standard error in the mean. The units of the mean - the reported power - are K^2, as the original maps are in units of K; taking the square of the Fourier transform of the brightness temperature maps gives a result in units of brightness temperature squared.

As the power spectra are calculated in pixel-based rings, a conversion from pixel scales to angular scales is necessary. The scales covered by any power spectrum depend on the size of the map analyzed, and the Fourier transform essentially inverts the scale so that the angular scale is simply $\theta = \theta_{\mathrm{map}}/d_{\mathrm{px}}$. θ_{map} is the width of the analyzed map in degrees, and d_{px} is the distance of the radial bins in pixels. The θ calculated in this way

are converted to multipole ℓ by the relation $\ell \approx 180°/\theta$, and any bad data points are discarded.
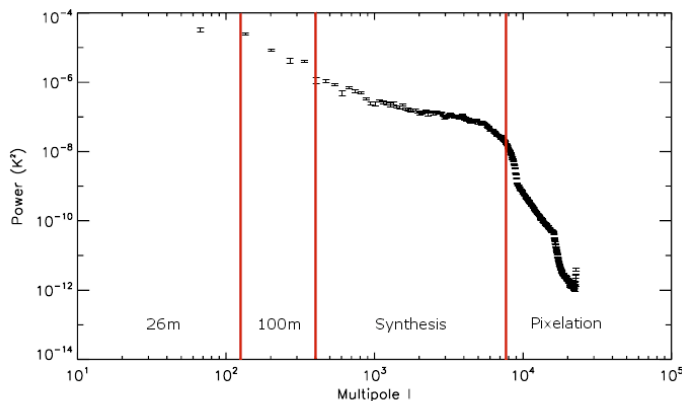
Figure 2.1: Sample power spectrum of a single 480x480 pixel submap centered at l = 120.7°, b = −1.7°. Power-law behaviour is evident at low multipoles, as is the tapering effect as $\ell \to 10^4$. Pixel effects are present beyond the taper, these are discussed in the text.

A representative power spectrum is given in Figure 2.1. The power decreases approximately linearly from the lowest sampled multipole to $\ell \sim \times 10^3$. On this log-log plot the linear portion is a power law. We consider the trend in this portion of the plot as a simple power law of the form $PS_X(\ell) \propto \ell^{-\alpha}$. The spectral index α of polarization power spectra is usually the result of interest, as in eg. Haverkorn et al. [2003], Giardino et al. [2002], Carretti et al. [2010], since it describes the distribution of power. Other features of the power spectra are rarely discussed, though Haverkorn et al. [2003] does mention a flattening at high multipoles due to noise in the image.

The applied taper discussed in Section 1.2.4 appears in Figure 2.1 from approximately $\ell \sim 3000$ to ~ 7700. Power beyond this multipole in Figure 2.1 cannot be a sampling of real signals, only pixel noise and other imaging effects. This is also evident in the plot itself, as the taper is replaced by these effects around $\ell \sim 10^4$. Any further analysis and plots of power spectra has been limited to $\ell \leq 7700$.

Only slightly visually evident in Figure 2.1, but easily found analytically, is a break in the power-law behaviour around $\ell \approx 10^3$. At multipoles lower than this value the power law is considerably steeper than at higher

multipoles. Unfortunately the applied taper confounds the interpretation of this flattening behaviour at high multipoles; nonetheless an investigation and interpretation is attempted in Section 2.6. In general the APS show complex behaviour across the multipole range and are not fully described by a single power-law with some noise flattening at high multipoles; a more detailed analytical model is necessary.

2.2 Model Fitting to APS

In order to determine accurate spectral index values while accounting for the flattening and taper effects at higher multipoles, we apply least-squares fitting to a given model. The flattening floor is modeled as a constant offset and the taper as a Gaussian apodization function, giving the following model:

$$P = \left[A + B\left(l\right)^{-\alpha}\right] \exp\left(-\frac{l^2}{2\sigma^2}\right). \tag{2.2}$$

The spectral index α determined by this model should be comparable to those in the literature, which generally fit only multipoles below $\ell = 1000$. Sample power spectra for a single galactic longitude are presented in Figures 2.2 and 2.3.

Two things of note become apparent in the attempted fits of the model to a single submap power spectrum as in Figures 2.2 and 2.3. First, it appears that the lowest sampled multipole has less power than the power-law fit expects in certain cases; and second, the Gaussian model taper does not accurately fit the observed taper at high multipoles. Variations in the different power spectra can reduce the discrepancy at the lowest multipole, but the non-Gaussian taper effect appears consistantly. Whether the effect is due to an incorrect model or a physically non-Gaussian taper is investigated in Section 2.7.

Multiple APS are calculated for each supermosaic so that variations in the fitting parameters across the galactic plane can be studied. A submap with 480 pixels to a side is taken from the full supermosaic, and the above analysis is applied to the submap. The submap is shifted by 60 pixels in the x and y directions, and analyzed again. This process is repeated until the entire supermosaic is sampled by submaps of 480 pixels which are themselves oversampled by a factor of 8. The supermosaics have a plate scale of $0.00556°$/px, so a 480 pixel submap has $\sim 2.7°$ to a side, and covers an area of $\sim 7.1^{°2}$. As the submap size limits the range of multipoles on the lower end, a 480 pixel submap allows multipoles down to $\ell \approx 67$

to be accurately sampled. Information at larger scales is still present in the images, but will contribute only to the total power in the image and not individual multipoles. We determine model parameters for each of the 480 pixel submaps, which we then combine in an image to determine the parameter trends across the supermosaics.

2.3 Point Source Removal

Point sources on the scale of the Synthesis Telescope beam size are apparent in the polarized intensity maps, and are found to add considerable power to the APS in which they are included. In some instances the presence of strong point sources leads to the model fit failing to converge to a solution, though this appears to be due to remaining imaging artifacts that were not removed fully in the cleaning process. Such image artifacts are prevalent especially around the strongest sources. Point sources are primarily expected to be extragalactic radio galaxies, showing no dependence on galactic latitude; a small portion of the point sources may be compact supernova remnants within the Galaxy itself, these being indistinguishable from extragalactic point sources. To study the diffuse polarized emission within our galactic plane the effects of such point sources should be mitigated, and this is accomplished in this investigation by their removal prior to the APS analysis.

We apply a standard Roberts edge enhancement filter to the polarization maps and any objects in the maps remaining above a threshold of 0.3K are marked for analysis and possible removal. Such objects are individually fitted with a two-dimensional Gaussian, and if the Gaussian full-widths at half maximum are less than 8 pixels (0.04°) the Gaussian fit is subtracted from the point source. The baseline of the fit remains, setting the previous point source to a brightness temperature comparable to its surroundings. It should be noted that such removal still leaves a feature in the polarization maps on the size scale of the telescope beam, leaving at least some of the original power in the map. If the attempted Gaussian fitting fails we discard the object as being a non point source and it remains in the polarization maps.

Figures 2.4, 2.5, and 2.6 show a comparison of APS before and after point source removal. All three sample regions are taken from the sixth supermosaic, with the first two having significant point sources in the area, while the third has only minimal point sources and serves as a comparison. The model parameters for the regions containing point sources are altered

by the removal of the point sources: the constant power offset parameter A is reduced while the power spectral index α is increased. Both effects are expected as the removal of the point sources significantly lowers the total power in the region, which has a larger relative impact at higher multipoles where the power is already lower. The reduction in small scale structure by removal of the point sources steepens the power spectra, which should then be representative of the diffuse emission in the Galaxy.

A comparison of the entire point-source-subtracted supermosaic 6 and a non-altered supermosaic 6 is presented in Figure 2.7. We note especially the lighter regions at $l = 174.7°$ and $l = 167.3°$, where the original supermosaic analysis shows sharp transitions to lower α. A single strong point source will be included in multiple submaps, thus reducing the spectral index in an area equivalent to a submap. The point-source-subtracted supermosaic shows more gradual transitions in these regions, indicating that the removal is effective. This behaviour is consistent throughout the supermosaics.

2.4   Maps of Spectral Indices

The maps of α determined from model-fitting to the supermosaic data are presented in Figures 2.8, 2.9, 2.10, and 2.11. The supermosaics are attached for comparison. Some information at the top and bottom edges of the supermosaics is lost due to the size of the submaps at 480 pixels. Smaller submaps would allow a more thorough sampling toward the edges of the maps, but the smaller size would also limit the multipole ranges in each power spectrum. In the maps of spectral indices, darker pixels indicate steeper power spectra, and thus excess power on large scales. Lighter pixels indicate regions with significantly more power on smaller scales. White pixels denote a failure of the model fitting procedure to converge to a reasonable solution. Most fitting failures are attributable to strong sources with residual imaging artifacts. Further discussion of distinct features in these α maps and their overall statistics is given in Section 3.1.

2.5   Linear Fitting to Flat Power

The extent of the flattening behaviour varies across the supermosaics, with some submap power spectra showing no flattening and others showing flat power across a wide range of multipoles. We parameterize the extent and flatness of the flattening effect with the linear slope in log-log space of the power spectra from $\ell = 1000$ to $\ell = 3000$. Linear-least-absolute-

deviation fitting is applied to this multipole range. The best-fit slope of this range is defined as the flatness parameter Δ. Submaps which show an increased flattening will have a smaller fitted slope in this region, thus a smaller flatness parameter Δ indicates a greater flattening effect.

2.5.1 Maps of Flattening

The same submap regions used for creating the spectral index maps are also used to create the flatness parameter maps, allowing us to sample the flatness of the power spectra across the galactic plane observed by the CGPS. The results of this are presented in Figures 2.12 and 2.13.

As in the power spectral index maps, information at the edges is lost due to the submap size. As the flattening occurs at multipoles sampled exclusively by the Synthesis Telescope it would be possible to use smaller submaps and still accurately measure its effects. This would allow us to reduce the information lost at the edges while also increasing the resolution of the sampling. This is not attempted here for consistency with the spectral index maps.

In the maps of flatness, data with $\Delta > 2$ indicates a region with a non-flattened power spectrum; for $1 < \Delta < 2$, the power spectrum visually shows some flattening; and for $\Delta < 1$ the flattening is obvious and significant. The maps are colourized with white representing the break from non-flattening to flattening; red colours indicate little flattening, and blue colours indicate significant flattening. Areas where the model fitting has failed are also white as in the spectral index maps.

2.6 Modeling Flat Power Contributions

The flattening observed in the angular power spectra is unexplained though not fully unexpected. Haverkorn et al. [2003] observes the flattening in power spectra of Stokes Q maps, and notes that it is noise, truncating the fitting at lower multipoles to avoid including its effects in the spectral index calcuations. While its appearance in the present data is expected, its extent is both unexpected and problematic. Prevalent for multipoles of $\ell > 10^3$, the flattening dominates the synthesis multipoles which range from $\ell \sim 400$ to $\ell \sim 8000$.

A power spectrum from a field observed with the synthesis telescope alone is shown in Figure 2.15. No data from the single-dish observations has been added, and the flattening is apparent out to the highest multipoles because the taper has not been applied. The extent of the flat portion of the

power spectrum is seen to cover most of the signal sampled by the Synthesis Telescope. The field plotted in Figure 2.15 is located at $l \approx 90$, $b \approx +1$, an area with significant flattening according to the Δ maps.

Noise is present in the data, but it should not overwhelm the signal to the extent demonstrated by the flattening effects. There are other possible sources of flat power spectra that may have some significance, and these are discussed alongside the effects of noise below.

2.6.1   Noise Contributions to APS

The stated sensitivity of the synthesis observations is 76 mK, from which the theoretical noise floor can be determined. Creating a noise map and taking its power spectrum is discussed in Section 2.7, analytical calculations of the noise power and an observational measure of the noise are given here.

The expected contribution of the noise power to the overall power spectrum can be calculated from the stated sensitivities of 76 mK in the synthesis data. The noise power depends on this sensitivity and the number of beams in the observed field:

$$PS_{noise} = 2 \frac{(0.076)^2}{N_{beams}} \tag{2.3}$$

The number of beams is approximated by a ratio of the pixels in the map and the number of pixels in a single synthesis beam on that map:

$$N_{beams} = w_{px}^2 / \frac{\pi \theta_{beam}^2}{8 \ln(2)} \tag{2.4}$$

For a regular submap of 480 pixels to a side ($w_{px} = 480$), the noise power is calculated to be $2.5 \times 10^{-8} \mathrm{K}^2$. This noise power is below the flattening observed in the power spectra.

An observational measure of the noise is also available as long as the field contains few imaging artifacts. The Synthesis Telescope at DRAO does not determine Stokes V directly, but it does create Stokes V maps during the data processing of Stokes Q and U maps that remain empty of real signal. However, the Stokes V maps do contain the noise and imaging artifacts present in Q and U. Calculating the power spectrum of Stokes V of a given Synthesis Telescope observation should give a measure of the noise power in that observation. Such a power spectrum is shown in Figure 2.16 for the observed field K3. The majority of the power spectrum is below a value of 10^{-8}, which when compared to the sample power spectrum in Figure 2.1 is found to be approximately an order of magnitude below the power at the flattening. The power spectrum is in fairly good agreement with the

above calculated value for the noise power. Noise does not appear to contain enough power to be responsible for the flattening effect.

2.6.2 Point Source Contributions to APS

To further investigate the flattening of the power spectra we created various model maps with point source emission and determined their angular power spectra. Compact unresolved extragalactic radio point sources that were not subtracted by the removal algorithm are an obvious candidate for providing a flat power spectrum due to the nature of their Fourier transforms. We consider signal in a single image pixel to be a two dimensional Dirac delta function, and calculate the Fourier transform of a delta function as follows:

$$\mathcal{F}\{\delta(x)\} = \int_{-\infty}^{\infty} \delta(x) \exp(-\imath 2\pi u x) \mathrm{d}x = 1. \tag{2.5}$$

Since the power spectrum is proportional to the square of the Fourier transform we conclude that the expected power spectrum will have equal power on all scales.

Actual radio observations of point sources do not generate a perfect Dirac delta function in a single pixel, instead smearing the signal across the beam of the telescope. As the flattening occurs entirely within the range of multipoles sampled by the Synthesis Telescope its number of pixels in a beam is determined:

$$N_{\mathrm{px}} = \frac{2\pi \theta_{\mathrm{beam}}{}^2}{8 \ln(2) \varrho^2} \tag{2.6}$$

The half-power beam width HPBW for the synthesis telescope is approximately $1'$, or $0.0167°$, and ϱ is the image scale in degrees per pixel. The supermosaics have an image scale of $0.00556°/\mathrm{px}$, so the synthesis telescope beam will cover 10.2 pixels. An observed point source can therefore be approximated with a Gaussian of the given HPBW and pixel coverage.

Placing a single source into an otherwise blank map of the same size as used for the submaps in Section 2.1 produces the power spectrum seen in Figure 2.17. The non-delta function behaviour is evident at high multipoles where the Gaussian appears while most of the power spectrum shows the flatness expected from a point source. The flux density of the point source was set to 0.4 Jy in order to match the observed powers in the flattening. This is equivalent to a peak surface brightness temperature of 6.7K. Polarized intensity emission as seen in Figures 5 to 7 in Landecker et al. [2010] is consistently below this brightness temperature, but the sum of multiple

point sources in the image may provide sufficient flux to reach such a temperature. As expected, the power spectrum is flat at the correct multipoles, and with a flux density of 0.4 Jy, also at approximately the correct power.

2.7   Investigating the Non-Gaussian Taper

The model-fitting diverges from the observed power spectra in the taper region. The taper applied to the synthesis data is a Gaussian that reaches 20% of its peak at the longest baseline of 617m, corresponding to a multipole of $\ell = 7700$. The other two telescopes contribute zero power at such a high multipole, thus having no effect on the taper or the accuracy of the fit. As seen in Figure 2.2, at the beginning of the taper the Gaussian fit has deficient power relative to the observed tapering. At the end of the taper, the highest multipoles, the Gaussian fit has excess power relative to the observed tapering. The Fourier transform of a Gaussian is also a Gaussian in the frequency domain, so the fitting should be accurate.

A perfectly Gaussian beam is fit well by a Gaussian model as seen in the model point source fitting in Figure 2.17, though this is an idealized situation. The actual beam changes shape as the declination of the observation increases; the synthesis beam has an actual resolution of 58" $\times$ 58" csc δ, where δ is the declination of the observed field. An elliptical trend in the supermosaics such as the effects of the synthesis beam losing circularity will create a non-circular Fourier transformed image as well. The averaging in radial bins would no longer correctly sample the Fourier transformed image in such a case, and this may be the cause of the apparent non-Gaussian taper. Figure 2.18 is the same point source as in Figure 2.17; however, the point spread function of the beam has been altered to an ellipse, with the major axis at double the minor axis of the ellipse, and the major axis rotated to 45° from the x axis. The model taper fails to correctly fit the point source's power spectrum, so this changing ellipticity across the supermosaics is the probable cause of the non-Gaussian tapering.
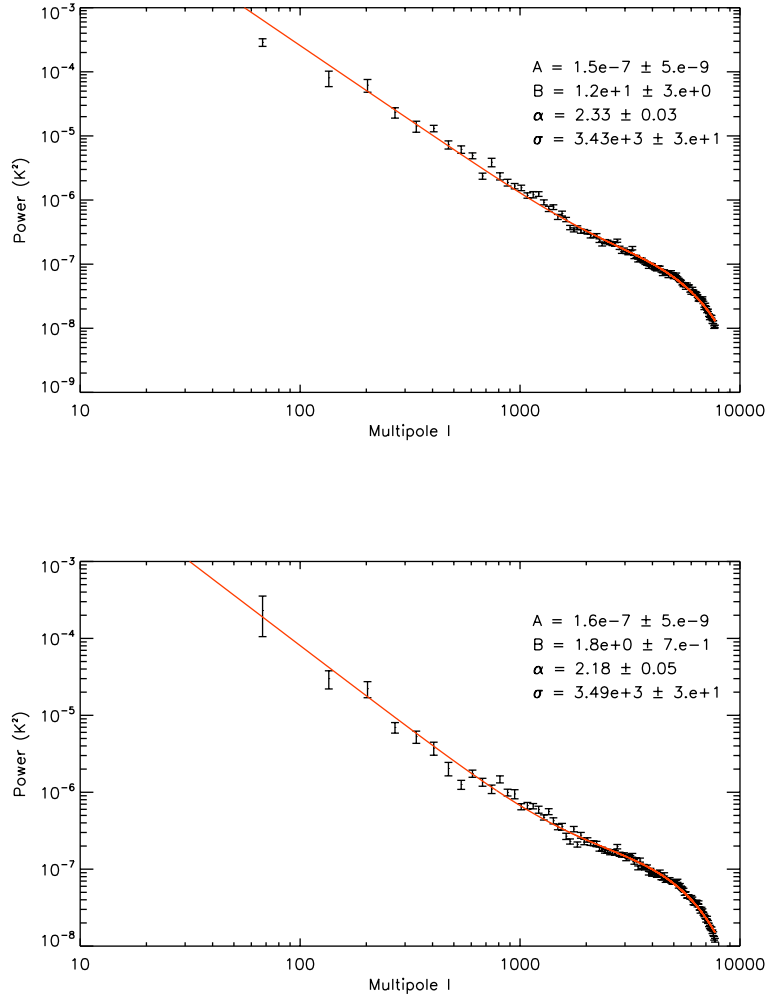
Figure 2.2: Sample power spectra of two 480x480 pixel submaps located at l = 150.0°, b = −1.3° and b = 0.0° respectively. The model of best fit is overplotted in red, and its parameters are given as well. The model consistently diverges from the data at the highest multipoles, where the taper appears ill-fit by the Gaussian model.

A = 1.6e−7 ± 3.e−9
B = 1.8e+1 ± 7.e+0
α = 2.65 ± 0.07
σ = 3.62e+3 ± 2.e+1

A = 1.6e−7 ± 2.e−9
B = 1.3e+2 ± 7.e+1
α = 3.07 ± 0.08
σ = 3.73e+3 ± 2.e+1
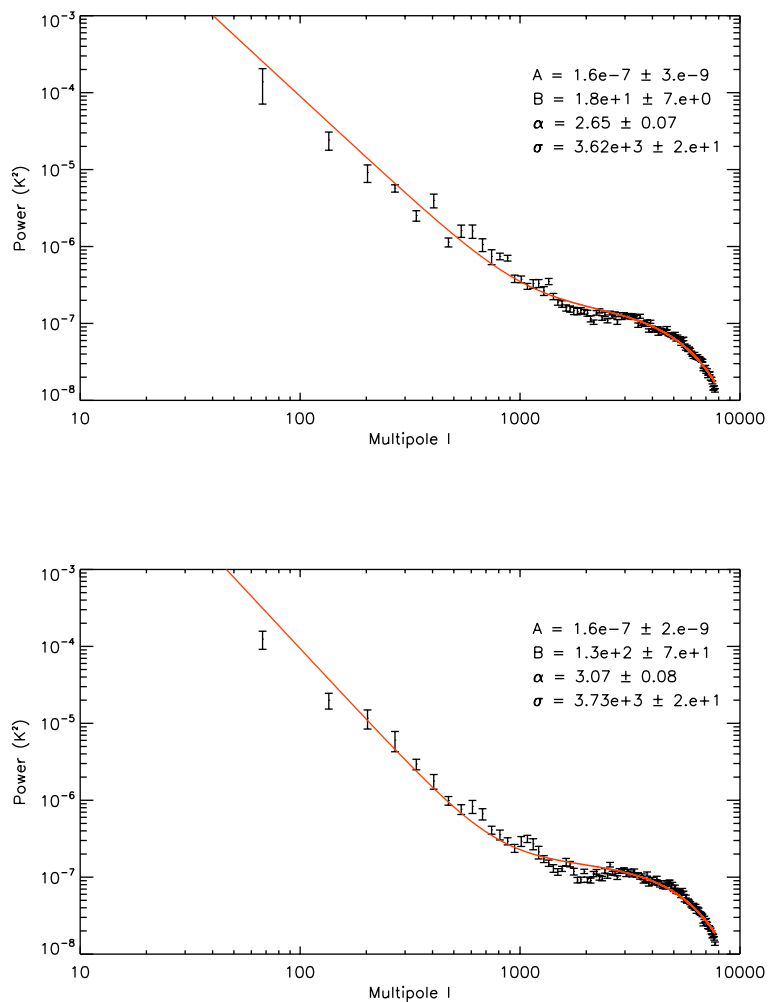
Figure 2.3: Sample power spectra of two 480x480 pixel submaps located at l = 150.0°, b = 1.3° and b = 2.7° respectively. The model of best fit is overplotted in red, and its parameters are given as well. The model consistently diverges from the data at the highest multipoles, where the taper appears ill-fit by the Gaussian model.

A = 3.0e−7 ± 3.e−8
B = 1.8e−2 ± 6.e−3
α = 1.37 ± 0.05
σ = 2.64e+3 ± 2.e+1

A = 3.2e−8 ± 6.e−9
B = 2.6e−1 ± 7.e−2
α = 1.84 ± 0.04
σ = 3.18e+3 ± 6.e+1
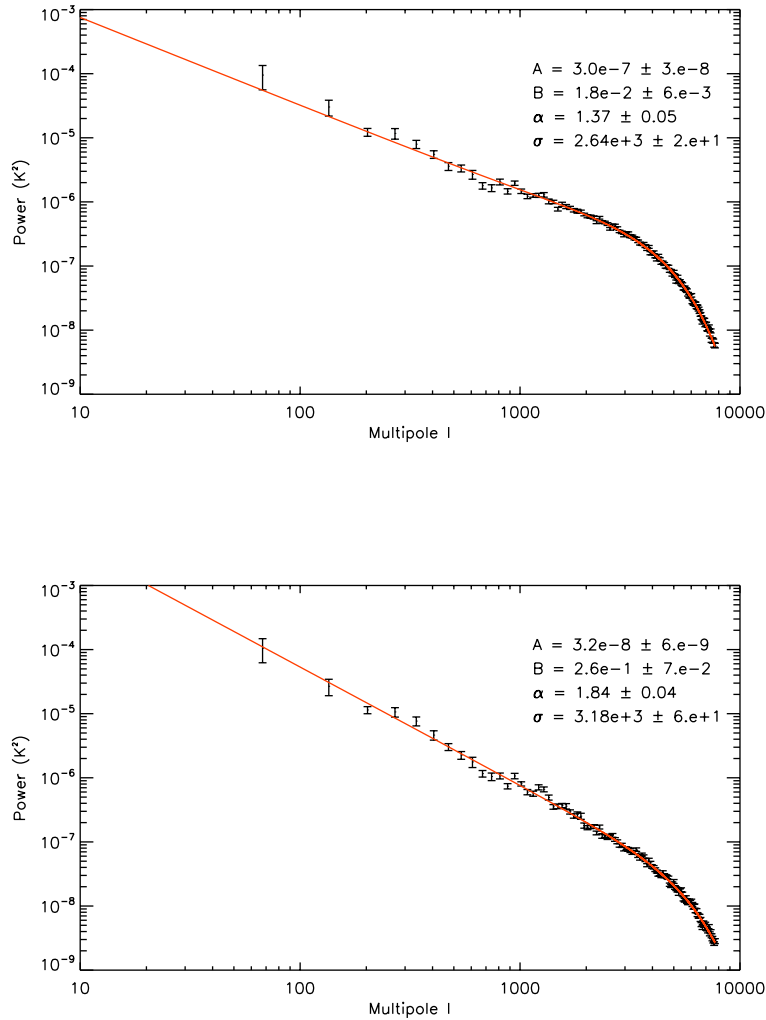
Figure 2.4: Angular power spectra and best-fit model with parameters for a submap centered at $l = 174.7°$, $b = −1.7°$. The submap of this region contains significant power in a point source. The top power spectrum is computed without point source removal, while the bottom power spectrum has undergone point source removal. Of note are the varying model parameters and the overall steepening of the power spectrum after point source subtraction.
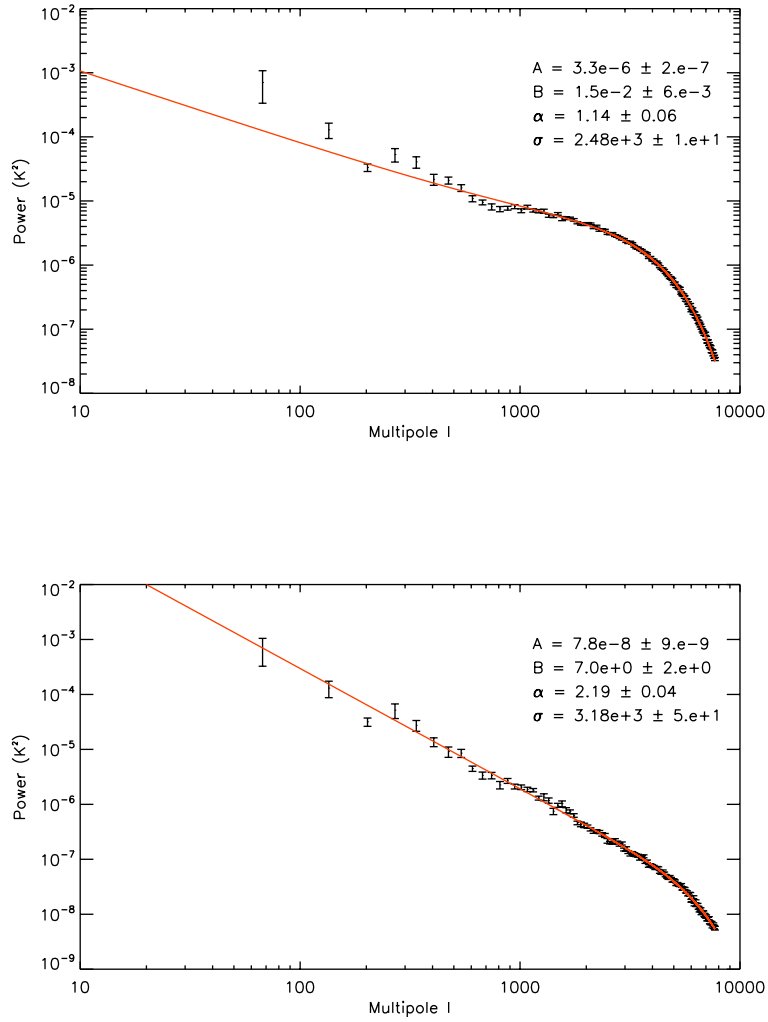
Figure 2.5: Angular power spectra and best-fit model with parameters for a submap centered at l = 167.3°, b = −1.3°. The submap of this region contains significant power in a point source. The top power spectrum is computed without point source removal, while the bottom power spectrum has undergone point source removal. The model fit is superior in the latter figure.
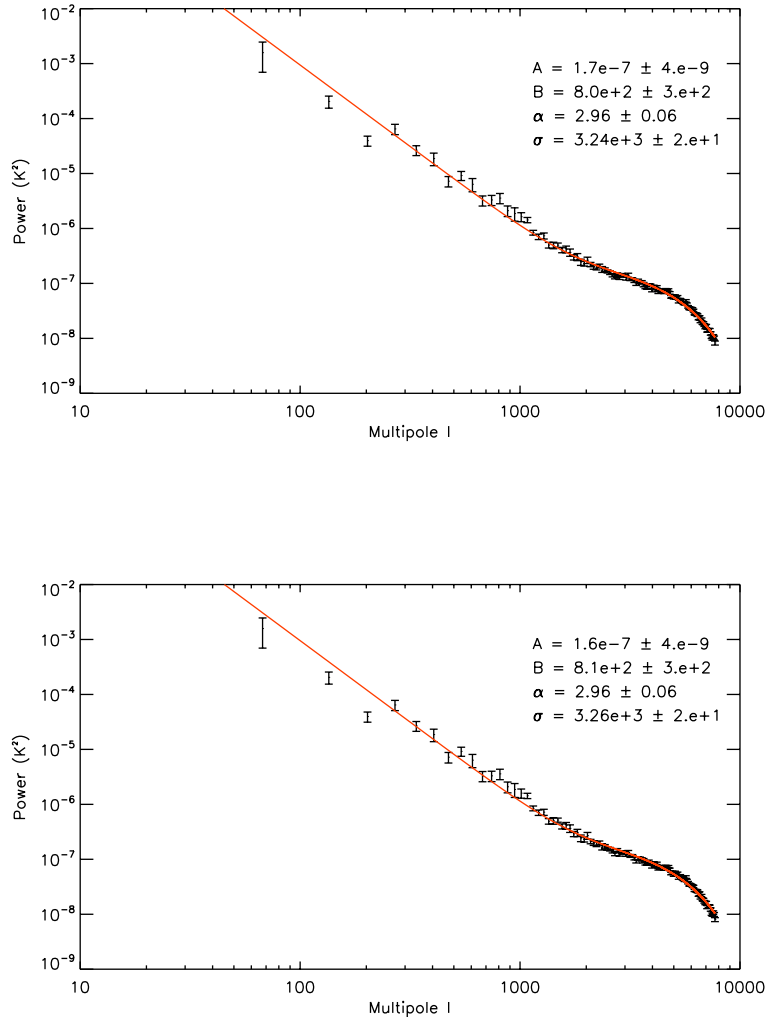
Figure 2.6: Angular power spectra and best-fit model with parameters for a submap centered at l = 156.7°, b = −1.7°. The submap of this region contains little power in point sources. The top power spectrum is computed without point source removal, while the bottom power spectrum has undergone point source removal. No significant changes occur in the model parameters.
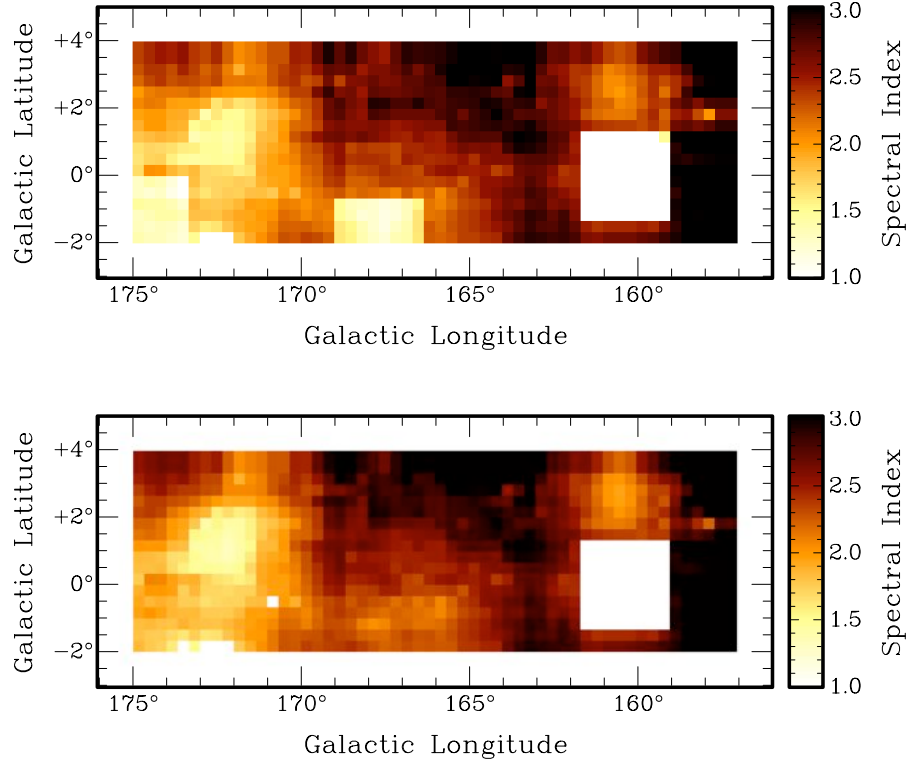
Figure 2.7: Power spectral index (α) maps created from the APS analysis of supermosaic 6. The top figure has not undergone point source removal, whereas the bottom figure has undergone point source subtraction. Evident in the top map are the sharp transitions in α due to the presence of bright point sources which dominate the power in the diffuse emission at large multipoles.
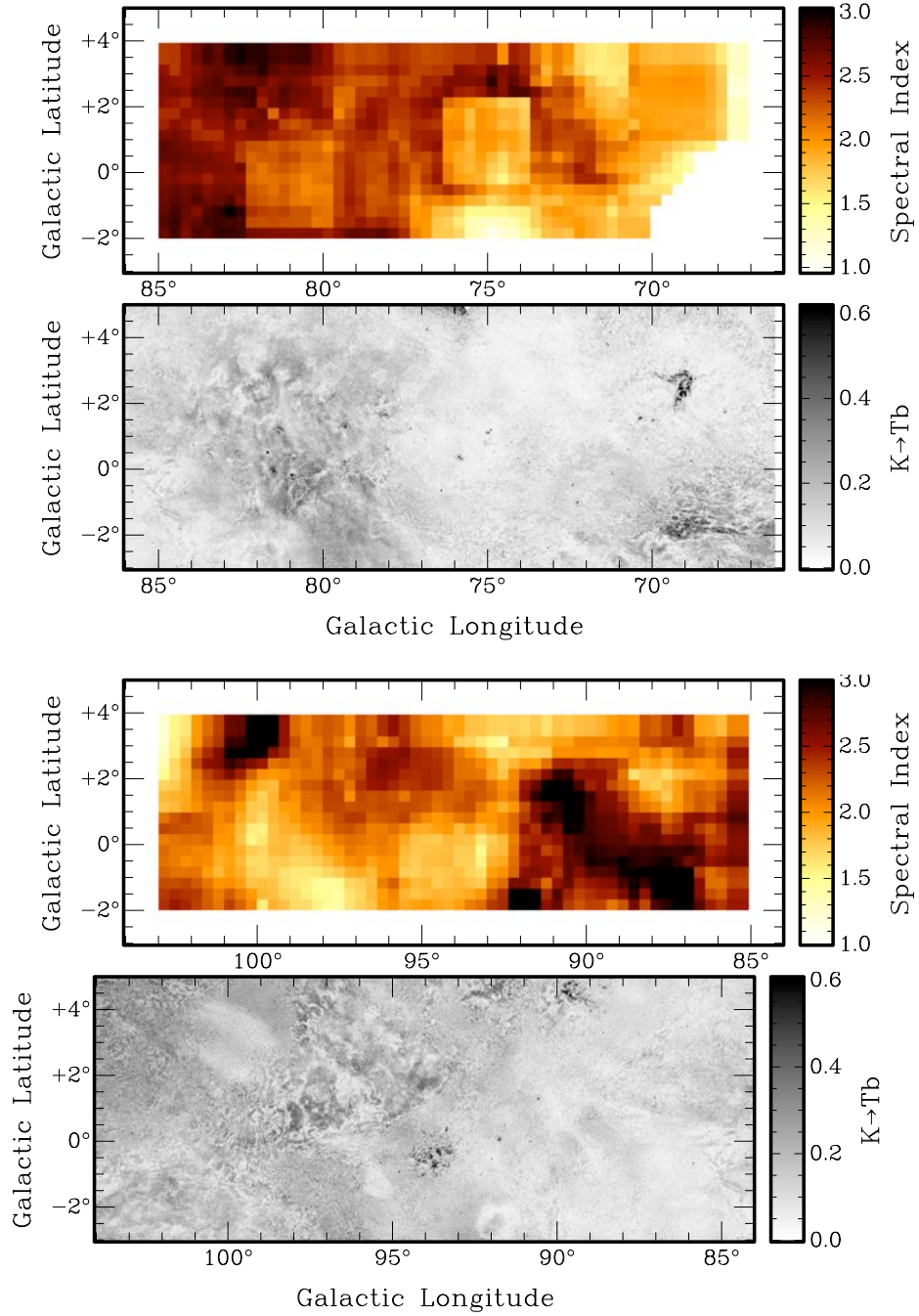
Figure 2.8: Maps of power spectral index values (α) in colour and polarized intensity in black and white for $l = 66°$ to $l = 104°$; all α values from model fitting to power spectra.
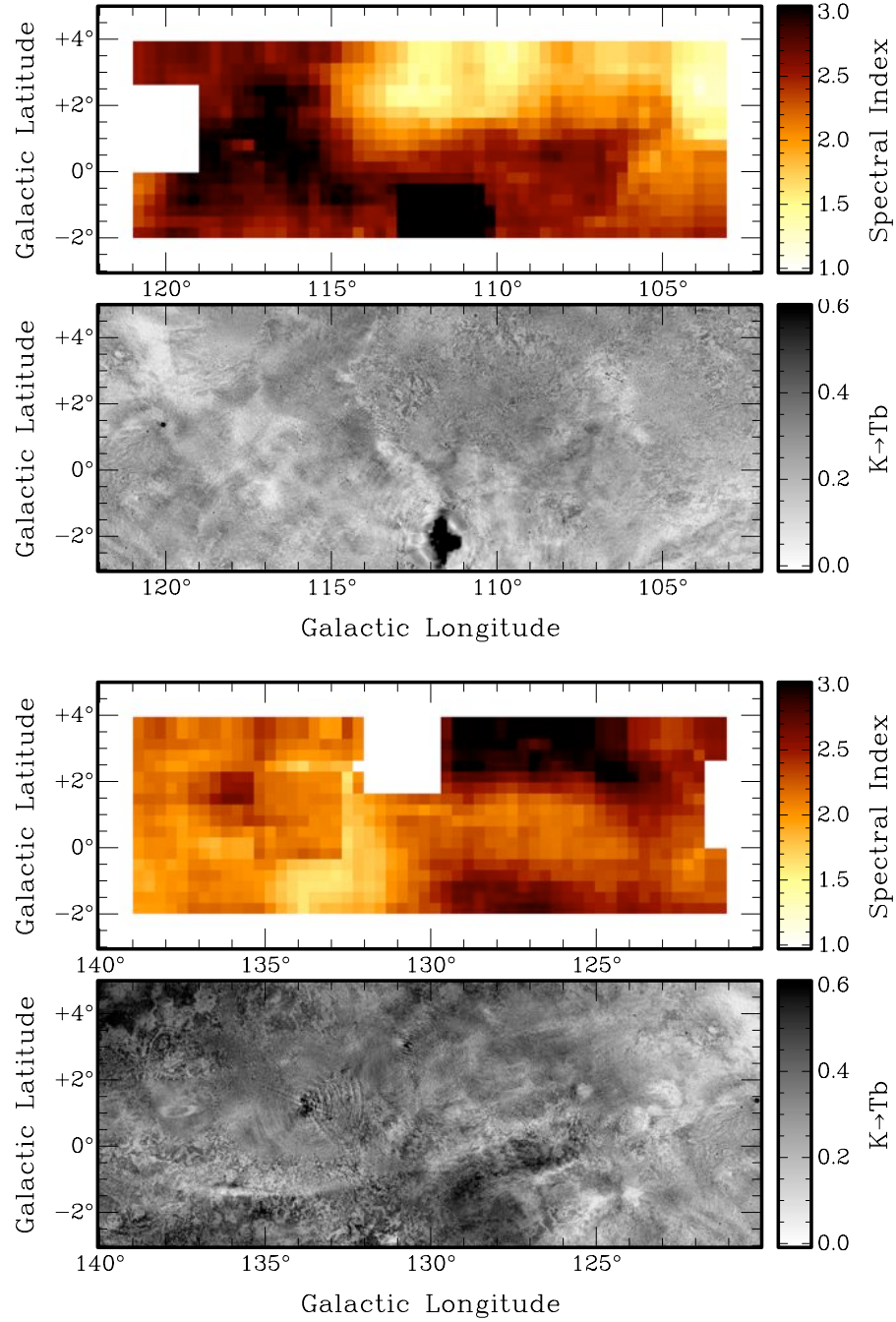
Figure 2.9: Maps of power spectral index values (α) in colour and polarized intensity in black and white for l $= 102°$ to l $= 140°$.
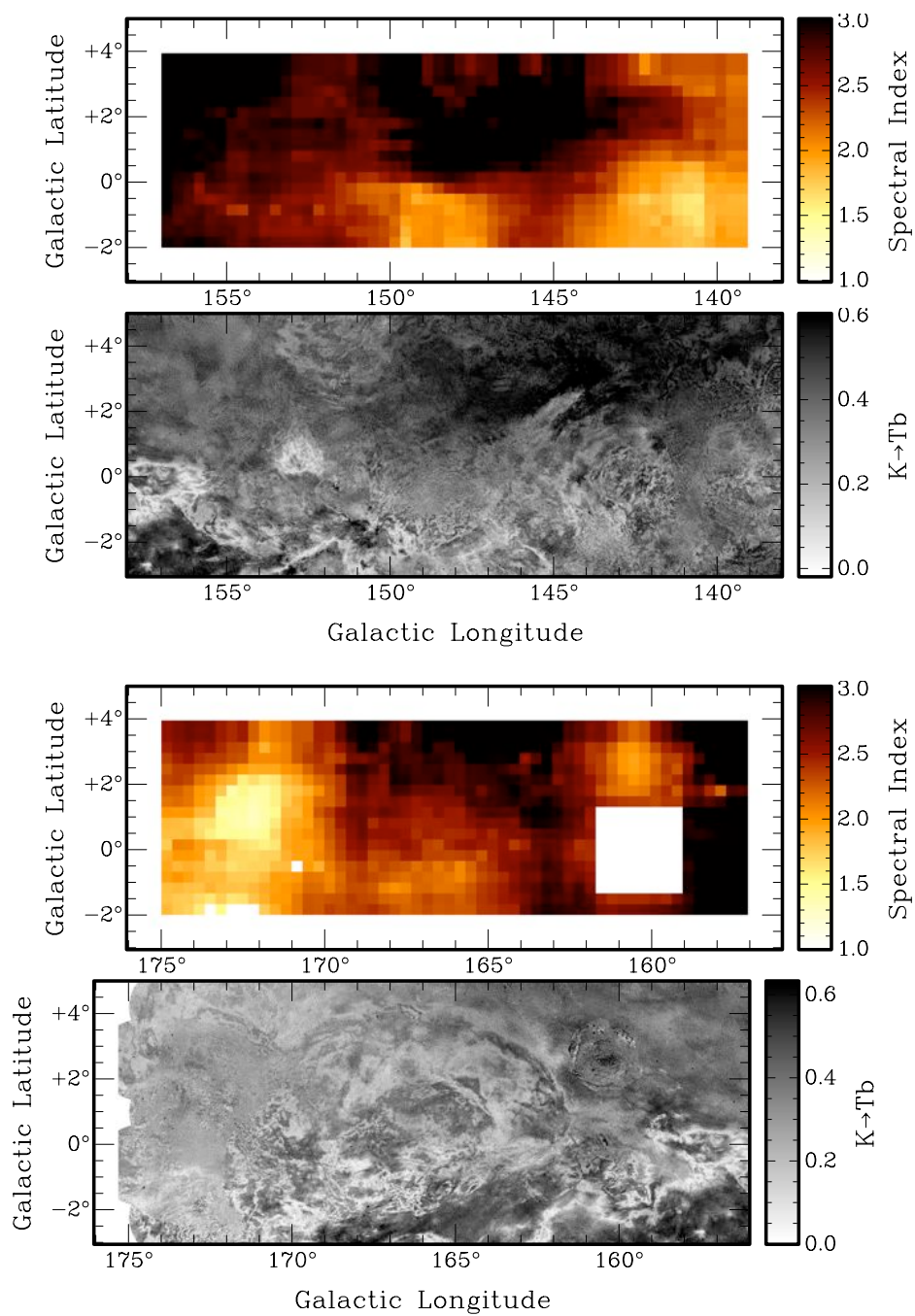
Figure 2.10: Maps of power spectral index values (α) in colour and polarized intensity in black and white for l $= 138°$ to l $= 176°$.
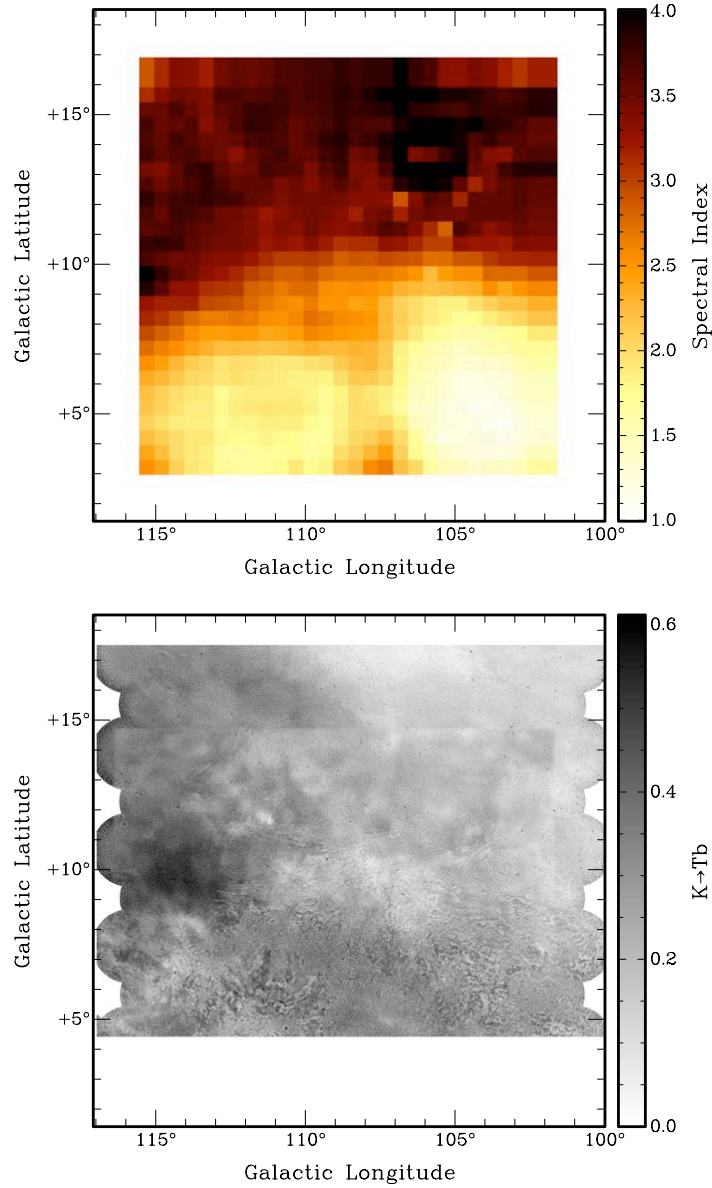
Figure 2.11: Power spectral-index (α) map for l = 101° to l = 116°, b = 3° to b = 17°. Polarized intensity map of the same region in black and white. This is the high-latitude extension of the CGPS. Note that the colourbar differs from those of the previous spectral index maps due to a greater range in values in this region. A clear break in α is evident at b = 10°.
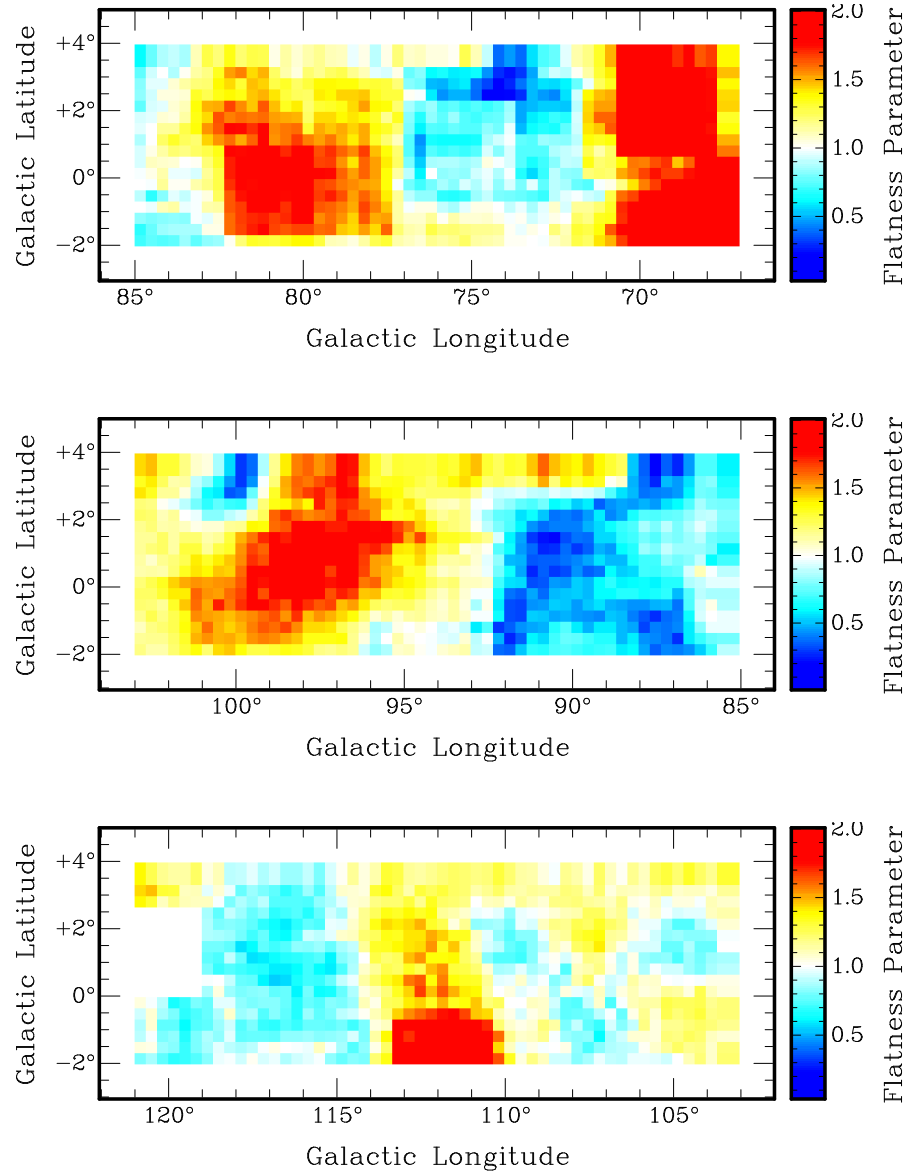
Figure 2.12: Flatness parameter (Δ) maps for $l = 67°$ to $l = 121°$. Higher values (red) indicate less flattening, while lower values (blue) indicate significant flattening.
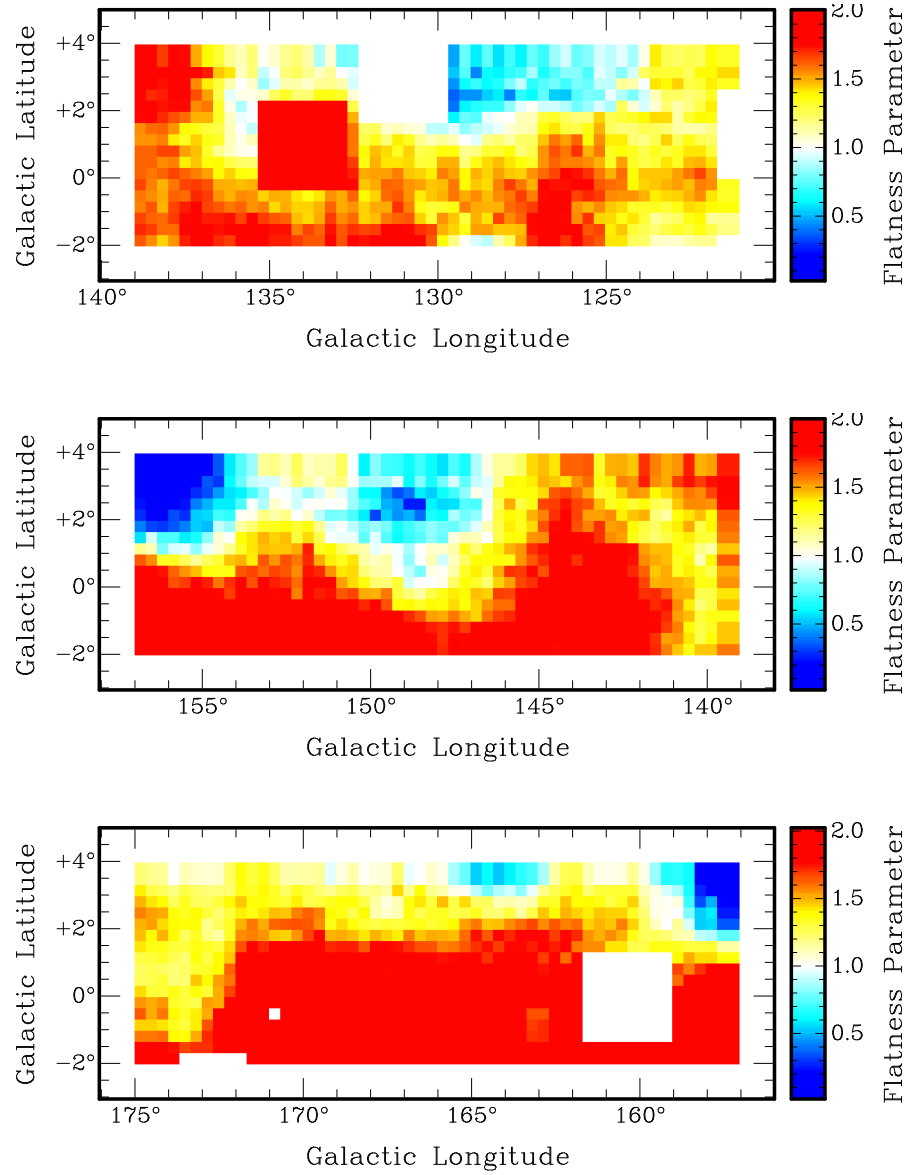
Figure 2.13: Flatness parameter (Δ) maps for l = 121° to l = 175°. Higher values (red) indicate less flattening, while lower values (blue) indicate significant flattening.
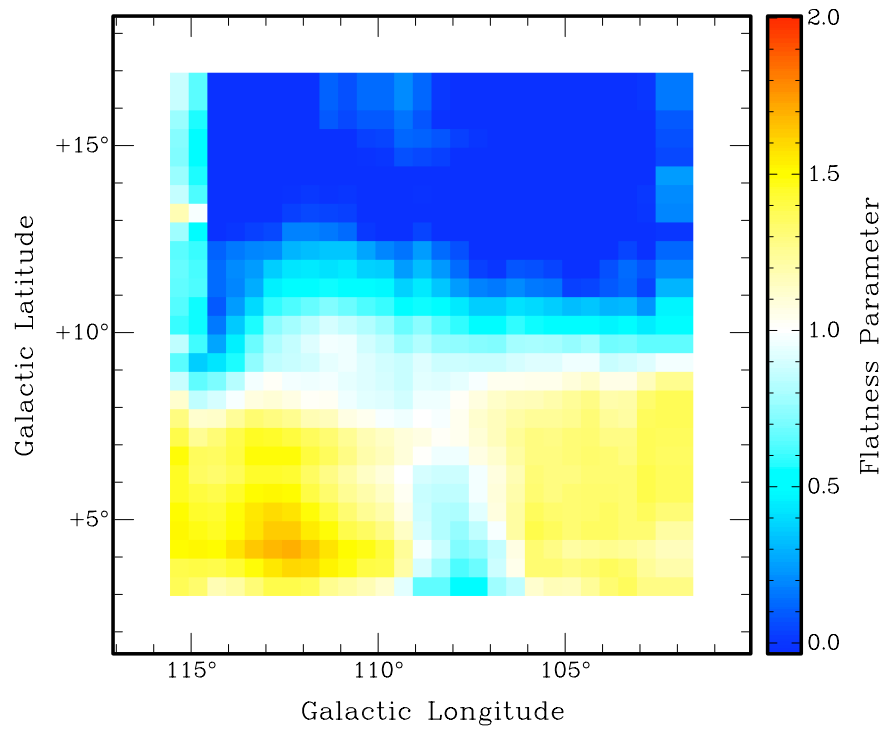
Figure 2.14: Flattening (Δ) map for l = 101° to l = 116°, b = 3° to b = 17°, the high latitude extension. As seen in the α map of the same region, a sharp transition is evident around b = 10°.
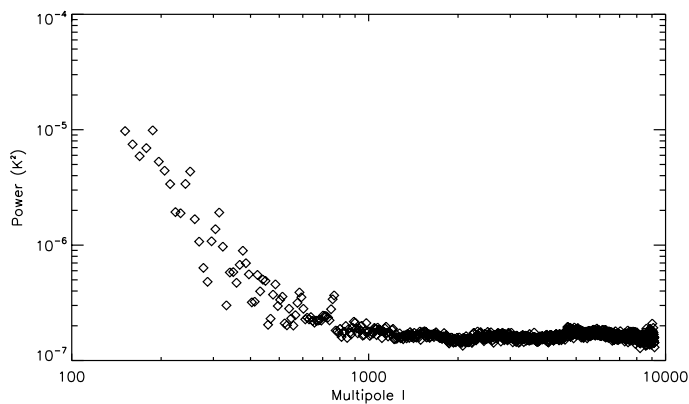
Figure 2.15: Power spectrum of a single synthesis field (K3) without added single-dish information. Of note is the flattening of the power spectrum for $\ell > 1000$; this flattening is also evident in the APS of the combined dataset.
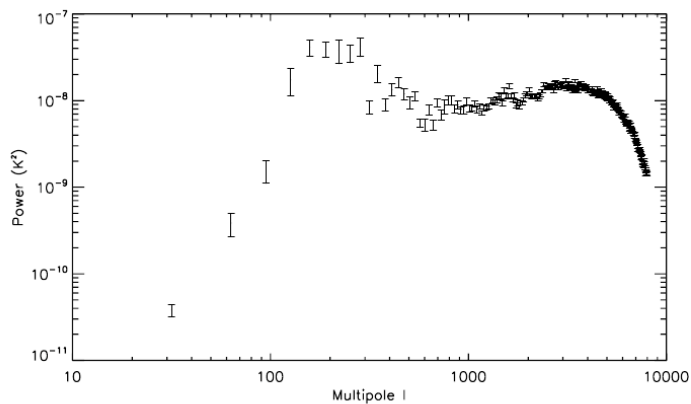
Figure 2.16: Power spectrum for a submap of the Synthesis Telescope observation of field K3 in Stokes V. This power spectrum represents the noise power present in this field, and by extension an approximation of the noise present in the supermosaics at synthesis multipoles.
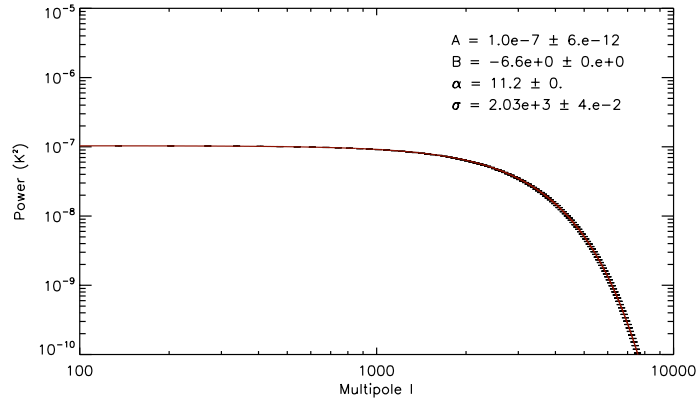
Figure 2.17: Angular power spectrum of a model point source with 0.4Jy of flux density. Map containing point source is 480 pixels to a side, with an image scale equal to that of the supermosaics at 0.00556°/px.
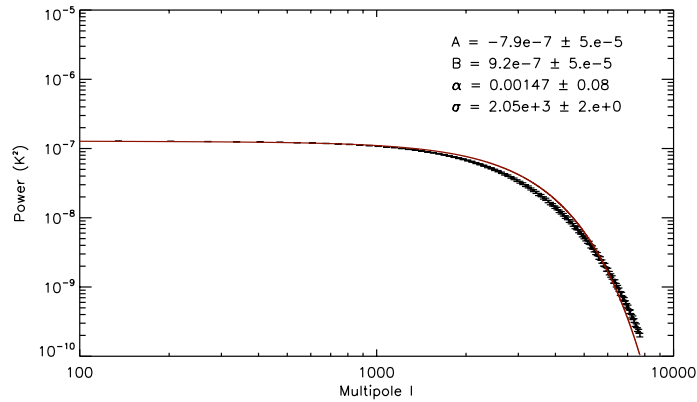
Figure 2.18: Angular power spectrum of a model point source with 0.4Jy of flux density. The observational effect of the Synthesis beam is approximated by rotating and elongating the point source into an ellipse. The model does not accurately fit the taper region for this elliptical beam shape.

33

Chapter 3

Discussion and Conclusion

3.1 Spectral Indices and Flattening across the CGPS

3.1.1 Model Failures

The model fitting procedure is seen to fail in four distinct major regions which generally correspond to extremely bright point sources in the polarized intensity maps of Landecker et al. [2010]. In order of increasing galactic longitude, these regions are outlined below. The first, visible at $l \sim 69°$, $b \sim -1°$ in Figure 2.8 does not correspond to a single bright source, but a collection of very bright non-point-source emission features. This model failing is unique in this, as all others are clearly attributable to a single bright source as indicated by their square (submap-sized) blank regions.

The second model fit failure occurs at $l \sim 120°$, $b \sim 0.4°$ in both Figures 2.8 and 2.9 due to its proximity to the edges of the relevant supermosaics. This appears to be caused by strong polarized emission from Tycho's supernova remnant. Visible in the polarized intensity maps as a very strong source of emission ($T \geq 0.6K$), the peak emission appears larger than a single beam of the Synthesis telescope and would thus escape the point-source removal algorithm. The addition of large amounts of power to the APS then causes the model fitting failure.

The third model fit failure occurs at $l \sim 131°$, $b \sim 3.1°$. The center of this failure region corresponds to object 3C58, a strong pulsar with an associated synchrotron nebula. The pulsar is not clearly visible in the polarized intensity map due to its location in a region of generally high polarized emission, but there are rings of image artifacts surrounding its location. It is more clearly evident in the total intensity map of the region. In this case the artifacts present in the polarization map would cause a model failure by introducing significant power on the size scales of the rings.

The fourth failure of the model to converge to a solution occurs at $l \sim 160°$, $b \sim 0.0°$. The radio galaxy 3C129 is a strong extragalactic source near this location, and it appears in the total intensity map as an extended

object. Though a strong point-like object that significantly alters the power spectra, 3C129 was not removed by the point source removal algorithm due to its extended nature in the map.

3.1.2 Spectral Index and Flattening Features

The regular component of the Galaxy's magnetic field is in the direction along $l = 85°$. This region is expected to have higher than average Faraday rotation and its resultant depolarization effects. However, the region also contains large-scale features that ensure high values of α. As the spectral index is measuring the balance of power between large and small scales, an increase in power in the small scale can be balanced by an increase in the large scales. The region around $l = 85°$ does however show an increase in flattening compared to its surroundings.

The Cygnus region peaks at $l = 80°$, and is visible in both the α and Δ maps. The spectral index increases slightly in the region, and is accompanied by a decrease in the flattening parameter. The Cygnus region is located in the middle of the longitudes that cover local features, which stretch from $l = 66°$ to $l = 100°$ [Landecker et al., 2010]. This region of local features has significant variation in both α and Δ, but is punctuated by a few distinct objects that alter the power spectra. The supernova remnant CTB80 at $l = 69°$, $b = 2.7°$ causes a strong decrease in flattening similar to the decrease seen around Cygnus; it also significantly steepens the power spectra as seen in the α map of the region.

The supernova remnant CTB104A at $l = 94°$, $b = -0.2°$ is not evident in either the α or Δ maps, so the presence of a supernova remnant does not guarantee an increase in α nor a decrese in Δ. However, CTB104A has visually less structure in the polarized intensity maps than CTB80, so its lack of effect is expected. The power spectra around Cassiopeia A at $l = 112°$, $b = -2°$ are very steep, with some of the highest α values in any of the maps. Unfortunately these power spectra are not indicative of the diffuse emission in the region due to the removal of Cassiopeia A in the polarized intensity maps and the presence of significant imaging artifacts [Landecker et al., 2010].

The superbubble GSH166-01-17 identified in Landecker et al. [2010] is not distinct from its surroundings in either the α or Δ maps. In general it is difficult to attribute changes in α or Δ to specific objects in the polarization maps. This is due to the ambiguity in whether the observed polarization features are due to intrinsically polarized emission in the background or due to the depolarization and vector-averaging as this emission passes through

foreground features. Examining the overall statistics and broader galactic trends of the results is more informative than attempting to identify individual features, as is often the case with polarization images due to their lack of resemblance to the total intensity maps in which objects are easily identified.

3.1.3 Spectral Index Statistics

The histogram in Figure 3.1 depicts the spread of spectral index values calculated from the Stokes PI supermosaics. Figures 3.2 and 3.3 give the histograms of the α values calculated from the Stokes Q and U maps respectively. These histograms do not contain values from the high latitude extension. The Stokes PI histogram peak is at a spectral index of $\alpha = 2.3$; Stokes Q derived values peak at $\alpha = 2.2$; Stokes U derived values peak at $\alpha = 2.5$. Stokes Q and U results are presented for comparison, but all discussion of spectral index features and large-scale trends are for Stokes PI derived spectral index value maps.
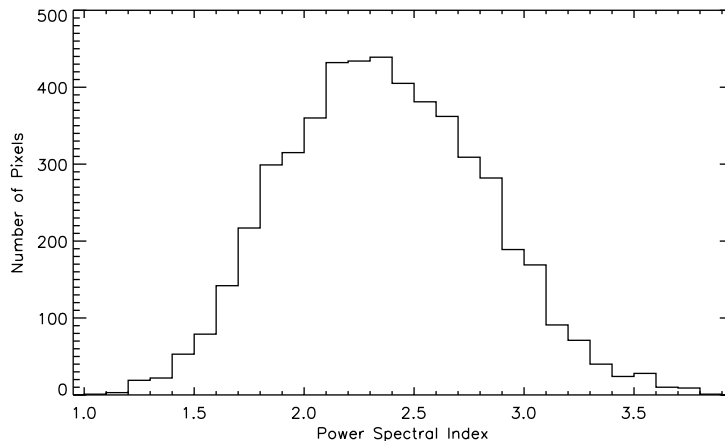
Figure 3.1: Histogram of power spectral-index values derived from Stokes PI supermosaics.

The result for the mode of α is similar to that observed in the Horologium and Auriga regions by Haverkorn et al. [2003], where the spectral indices are found to be 2.34 ± 0.31 and 2.20 ± 0.24 respectively. The Haverkorn et al. [2003] values come from polarization measurements at 350 MHz with a synthesis telescope suffering from missing short spacings, and at a much lower frequency where Faraday rotation effects are expected to be more
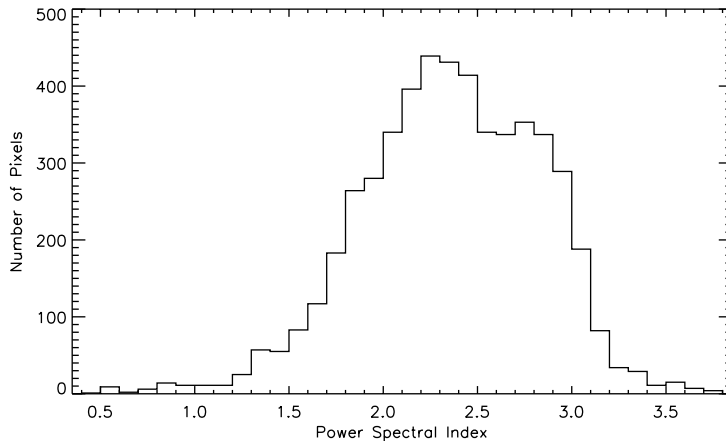
Figure 3.2: Histogram of power spectral-index values derived from Stokes Q supermosaics.

significant; the fields are also at galactic latitudes of 7° and 16° respectively, so direct comparisons may not be accurate.

Observations around 2.4 GHz by Giardino et al. [2001] with a single-dish telescope able to sample up to multipole $\ell = 1000$ give similar spectral indices as well, with a mean value of $\alpha = 2.43 \pm 0.05$. Similar latitudes are covered as in the present study, but the higher frequency is expected to be less affected by Faraday rotation, resulting in steeper power spectra as more power remains at larger scales. A later set of observations at 2.4 GHz by Carretti et al. [2010] over galactic latitudes from the South Galactic Pole to the galactic meridian found similarly steep angular power spectra at latitudes of $b > 40°$. However, for $b < 20°$, the regions most applicable to the results presented in this thesis, Carretti et al. [2010] find an average spectral index of $\alpha = 1.8$.

The above comparisons suffer from being at different frequencies where the effects of Faraday rotation may be different. Observations at 1.4 GHz have been less complete at sampling galactic latitudes, but some studies exist. Carretti et al. [2005] studies regions at $b = 63°$ and $-40°$. Their results are lower than those here, with average spectral indices of $\alpha \approx 1.7$ and 2.0 respectively. Carretti et al. [2010] notes that there is a transition from the galactic disk to the halo between $b = 20°$ and $40°$, so these spectral indices are sampling visibly different polarization skies.

Directly comparable to the results presented in this thesis is the analysis
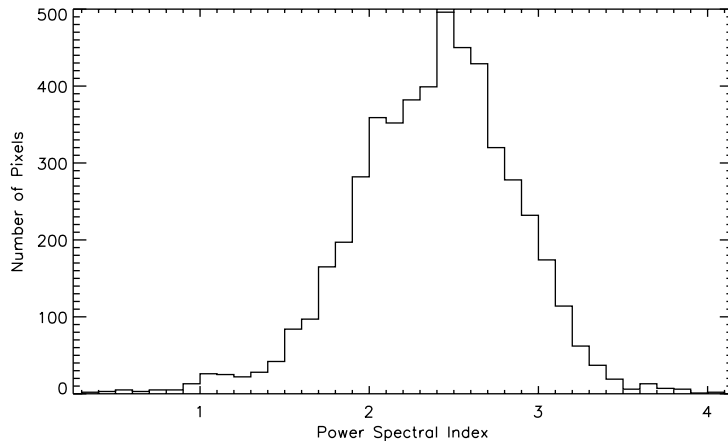
Figure 3.3: Histogram of power spectral-index values derived from Stokes U supermosaics.

by Tucci et al. [2002] of the Southern Galactic Plane Survey test field of 28 deg^2 located on the galactic plane, observed at 1.4 GHz. They determine a spectral index of $\alpha \approx 1.7$, lower than the mode of the current results but not beyond the bounds of the histogram. Similar regions exist in the data analyzed in this thesis, so this lower value for α may not be representative of all southern galactic plane regions. La Porta and Burigana [2006] use single-dish data to determine spectral indices at 1411 MHz. They report spectral indices of $\alpha \sim 2-3$ for a broad latitude coverage. It should also be noted that the point-source removal is currently unique to this thesis, the effect of which would be an increase of α in regions where point sources were previously significant.

The high latitude region has two populations of α values, with a clear break at a galactic latitude of b = 10°. Figure 3.4 shows the histogram of the α values in the high latitude region. For b > 10°, the most common spectral index is $\alpha = 3.8$. For latitudes closer to the galactic meridian the spectral indices are considerably lower with a mode of $\alpha = 1.9$. Landecker et al. [2010] notes that the polarization map of the high latitude extension has a visual separation between b = 8° and b = 10°; small-scale structure is visible for b < 10°, and is absent for b > 10°. This visual separation is analytically verified by our results for α which suggest the presence of local features for b < 10° and a regular component of the magnetic field that remains present above this latitude. The latitude extension results are

comparable to those of Carretti et al. [2010], who find a transition from disk to halo in the region $20° < b < 40°$. Both our results and those of Carretti et al. [2010] are limited by the ranges of galactic longitudes covered. Local features not representative of the overall galactic trend may be present in either set of observations. A full observation of the galactic plane at larger galactic latitudes would indicate where the true transition lies.

Covariances between the model parameters are also determined in each fit, and their averages across all calculated power spectra are given here. The strongest covariance is between α and B, at an average of 0.995. σ and A have an average covariance of -0.927, while the other covariances are insignificant and vary between 0.5 and 0.7.
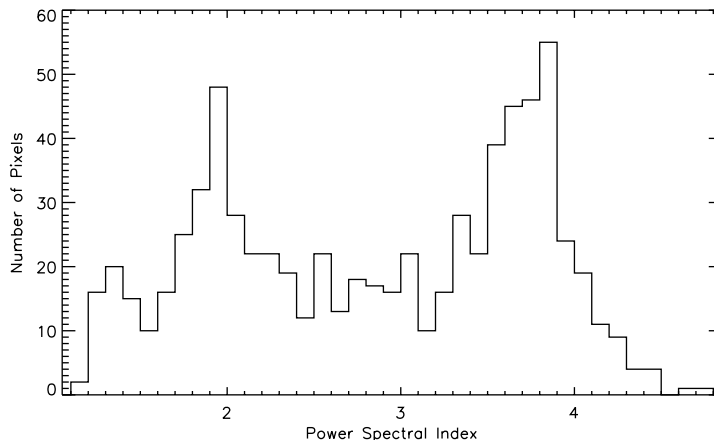
Figure 3.4: Histogram of α values from the high latitude extension of the CGPS in Stokes I. Two peaks are visible due to the sharp increase in α at b = 10°.

The values determined in this investigation are within the accepted ranges of spectral index values in the literature. Though there is no clear accepted value for the spectral indices at 1.4 GHz for low galactic latitudes, it appears that the presented values are on the steeper end when compared to higher latitude regions. It should be noted that there is no consensus on the appropriate multipole range to be used to calculate spectral index values, and most authors arbitrarily choose the range such that non-linear portions of the power spectra are entirely excluded. Our work has attempted to include the full range of the power spectra by utilizing a model of best fit, and thus our results are expected to differ from those in the literature.

3.1.4 Spectral Index and Galactic Latitude

Figure 3.5 shows how the spectral index changes with galactic latitude in steps of $b = 0.1°$. Median values for the spectral index are given at each latitude to avoid outlier effects of bad model fits. The spectral index values trend upwards as galactic latitude increases. This indicates a steepening of power spectra as observations move away from the galactic equator; observationally this describes a shifting of power from smaller to larger scales in the polarization maps. This trend may vary significantly with specific subsections of longitudes due to locally varying features; the average over the entirety of the longitudinal range nonetheless appears significant.
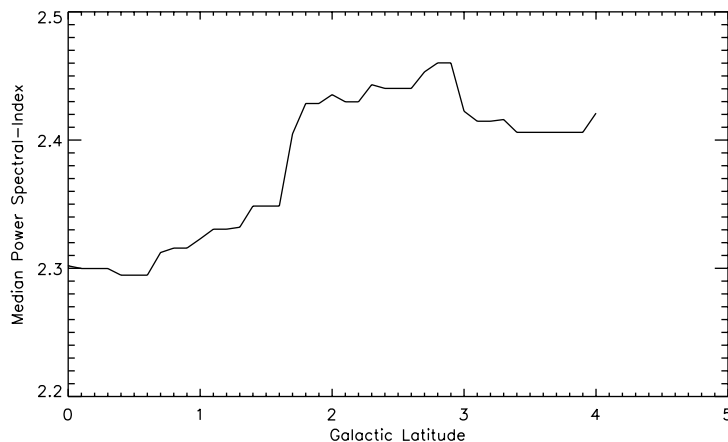
Figure 3.5: Power spectral index α plotted versus galactic latitude b to view averaged trends across the visible galactic disk.

Carretti et al. [2010] and Haverkorn et al. [2003] are observations with a broad enough range of latitudes to determine a trend. Carretti et al. [2010] finds a general increase of the spectral index α from $b = 0°$ to $b \sim -60°$, and a decrease of the spectral index from $b \sim -60°$ to $b \sim -90°$. Haverkorn et al. [2003] finds a decrease in the spectral index with increasing galactic latitude up to $b = 25°$, however the latitudes below $b = 10$ are not well sampled, and there is no change from $b = 5°$ to $10°$. The results of the present investigation do not disagree with either of these previous studies, though they themselves disagree for $b = 10°$ to $25°$. As the spectral indices seem to respond strongly to individual features that may be physically close, trends with galactic latitude may be overwhelmed easily by local features. If local features dominate then our investigation may be the most accurate

measure of the broader latitudinal trend due to the unprecedented range of longitudinal coverage.

3.1.5 Flattening Statistics

A histogram of the Δ values is included in Figure 3.6, and is seen to peak at $\Delta = 1.3$. The histogram also indicates that the majority of the power spectra analyzed did not have a significant flattening trend. Figure 3.7 is the histogram of Δ values for the high latitude extension; similar to the α histogram of this region, this histogram appears to contain two distinct populations, one with very significant flattening and one with generally insignificant flattening. As seen previously in Figure 2.14 the flattening trend is significant for b > 10°. The obvious anticorrelation of α and Δ in the high latitude region is not supported by the results of the supermosaic analyses.

3.1.6 Flattening and Galactic Latitude

Figure 3.8 depicts the flattening trend as a function of galactic latitude for the supermosaics. Median values were found in 0.1° latitude intervals. As an increase in flatness parameter Δ signifies a decrease in the amount of flattening, it appears that the strength of the flattening effect increases as observations move away from the galactic equator. The sudden drop in Δ at $b \approx 1.9°$ comes shortly after a sudden increase in α at $b \approx 1.6°$. Some correlation is expected, but the significance of this transition is unknown. No similar measurements exist in the literature, so these conclusions are presented without verification or support.

If the flattening is due to remaining point sources in the maps we would not expect a dependence on galactic latitude, as the point sources are extragalactic and should be uniformly distributed across the sky. If the flattening is due to noise in the maps, there is no reason to expect an increase with galactic latiude either, so the observed trend does not support a specific cause of the flattening. Both the noise and background point sources would produce a noise-like power spectrum at a constant power as discussed in Section 2.6.2. The total power in polarized emission increases towards the galactic equator, so the constant power from noise or point sources would have proportionally less effect at lower latitudes, possibly falling below the actual power of the Faraday-rotated structure in the maps. This could explain the latitude dependence of the flattening while allowing it to keep a constant power due to either noise or remaining point sources. Unfortunately little correlation was found between the model parameter A and the
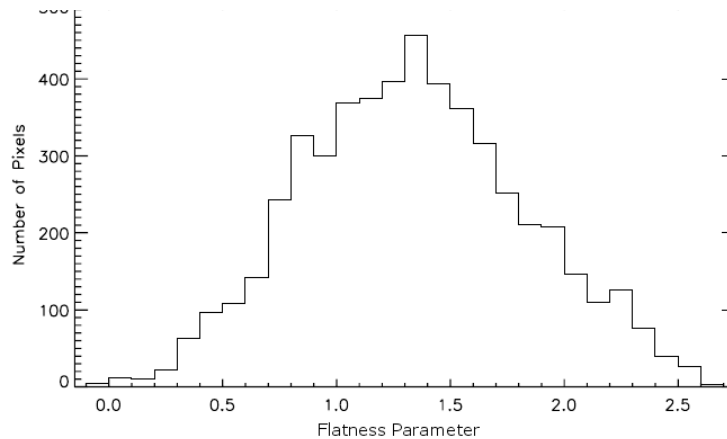
Figure 3.6: Histogram of Δ values derived from the Stokes I supermosaics.

flattening parameter Δ.

3.2 Conclusion

Power spectral indices were calculated for the entirety of the CGPS polarization dataset presented by Landecker et al. [2010]. Unparalleled in its galactic coverage and resolution, the survey is truly set apart by its inclusion of all angular scales. By combining single-dish and synthesis telescope data the CGPS can accurately measure polarization that would otherwise be missing the largest of structures. The calculated spectral indices constitute the largest such analysis, and the first mapping of spectral indices. The results presented here determine a dependence of the spectral indices on galactic latitude, with a shift of power to larger scales as observations move away from the galactic equator. The high latitude extension of the CGPS clearly shows a transition in power from smaller scales to larger scales at the galactic latitude of b = $10°$.

Instrumental and observational effects of the data were also examined, such as the non-Gaussian taper effect that may need to be corrected for future studies of the CGPS maps. A flattening of power spectra was also observed for $l > 1000$, covering most of the multipoles sampled by the Synthesis Telescope. Investigation of this flattening indicates an increase in flattening as galactic latitude increases, but its cause remains uncertain. It is unlikely to be noise or extragalactic point sources if the latitude dependence
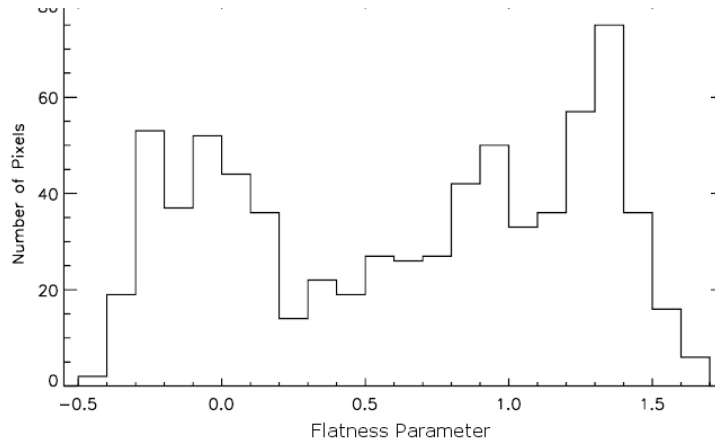
Figure 3.7: Histogram of Δ values derived from the Stokes I map of the high latitude region.

is valid, and quantifying the effects of Faraday depolarization in causing the flattening are difficult.

The polarized sky still holds much to be discovered, and a full classification of the features in the polarized sky may soon be possible as large surveys such as the CGPS reveal polarization structure on all scales. Decoupling small-scale magnetic field variances and electron densities from the regular component of the magnetic field remains difficult at 1.4 GHz, and is not attempted in this thesis; nonetheless, significant statistical results regarding the polarized sky have been determined and presented.
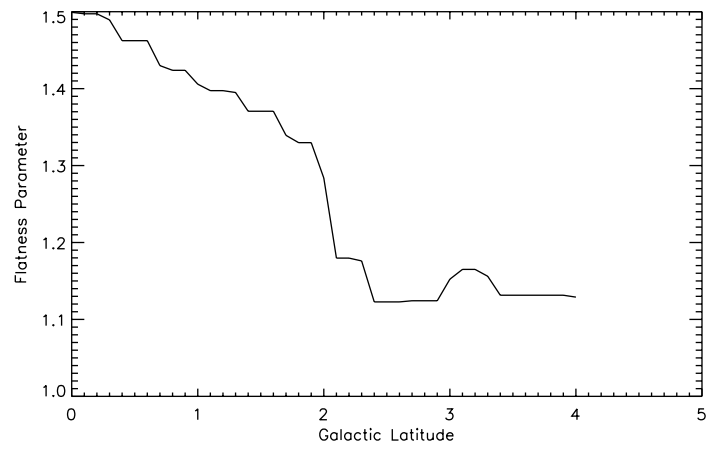
Figure 3.8: Flatness parameter Δ plotted versus galactic latitude b.

Bibliography

R. Beck. Galactic and extragalactic magnetic fields - a concise review. *Astrophysics and Space Sciences Transactions*, 5:43–47, October 2009.

Bernard F. Burke. *An Introduction to Radio Astronomy*. Cambridge University Press, New York, New York, 3rd edition, 2010.

E. Carretti, G. Bernardi, R. J. Sault, S. Cortiglioni, and S. Poppi. High Galactic latitude polarized emission at 1.4 GHz and implications for cosmic microwave background observations. *Monthly Notices of the Royal Astronomical Society*, 358:1–12, March 2005. doi: 10.1111/j.1365-2966.2005.08761.x.

E. Carretti, M. Haverkorn, D. McConnell, G. Bernardi, N. M. McClure-Griffiths, S. Cortiglioni, and S. Poppi. The Parkes Galactic Meridian Survey: observations and CMB polarization foreground analysis. *Monthly Notices of the Royal Astronomical Society*, 405:1670–1689, July 2010. doi: 10.1111/j.1365-2966.2010.16608.x.

J.J. Condon and S.M. Ransom. Nrao essential radio astronomy course, 04 2011. URL http://www.cv.nrao.edu/course/astr534/ERA.shtml.

G. Giardino, A. J. Banday, P. Fosalba, K. M. Górski, J. L. Jonas, W. O'Mullane, and J. Tauber. The angular power spectrum of radio emission at 2.3 GHz. *Astronomy and Astrophysics*, 371:708–717, May 2001. doi: 10.1051/0004-6361:20010384.

G. Giardino, A. J. Banday, K. M. Górski, K. Bennett, J. L. Jonas, and J. Tauber. Towards a model of full-sky Galactic synchrotron intensity and linear polarisation: A re-analysis of the Parkes data. *Astronomy and Astrophysics*, 387:82–97, May 2002. doi: 10.1051/0004-6361:20020285.

M. Haverkorn, P. Katgert, and A. G. de Bruyn. Characteristics of the structure in the Galactic polarized radio background at 350 MHz. *Astronomy and Astrophysics*, 403:1045–1057, June 2003. doi: 10.1051/0004-6361:20030464.

M. Haverkorn, P. Katgert, and A. G. de Bruyn. Structure in the polarized Galactic synchrotron emission, in particular "depolarization canals". *Astronomy and Astrophysics*, 427:549–559, November 2004. doi: 10.1051/0004-6361:200400051.

R. Kothes and T. L. Landecker. Polarization Structures in the Canadian Galactic Plane Survey: A Multispectral View. In B. Uyaniker, W. Reich, & R. Wielebinski, editor, *The Magnetized Interstellar Medium*, pages 33–38, February 2004.

J. D. Kraus. *Radio Astronomy*. Cygnus-Quasar Books, 2nd 1986.

L. La Porta and C. Burigana. A multifrequency angular power spectrum analysis of the Leiden polarization surveys. *Astronomy and Astrophysics*, 457:1–14, October 2006. doi: 10.1051/0004-6361:20054321.

T. L. Landecker. The Role of Magnetic Fields in the Interstellar Medium of the Milky Way. , pages 80–+, July 2011.

T. L. Landecker, P. E. Dewdney, T. A. Burgess, A. D. Gray, L. A. Higgs, A. P. Hoffmann, G. J. Hovey, D. R. Karpa, J. D. Lacey, N. Prowse, C. R. Purton, R. S. Roger, A. G. Willis, W. Wyslouzil, D. Routledge, and J. F. Vaneldik. The synthesis telescope at the Dominion Radio Astrophysical Observatory. *Astronomy and Astrophysics Supplement*, 145:509–524, September 2000. doi: 10.1051/aas:2000257.

T. L. Landecker, W. Reich, R. I. Reid, P. Reich, M. Wolleben, R. Kothes, B. Uyaniker, A. D. Gray, D. Del Rizzo, E. Furst, A. R. Taylor, and R. Wielebinski. A Survey of the Polarized Emission from the Galactic Plane at 1420 MHz with Arcminute Angular Resolution. *ArXiv e-prints*, April 2010.

W. Reich, E. Fürst, P. Reich, B. Uyaniker, R. Wielebinski, and M. Wolleben. The Effelsberg 1.4 GHz Medium Galactic Latitude Survey (EMLS). In B. Uyaniker, W. Reich, & R. Wielebinski, editor, *The Magnetized Interstellar Medium*, pages 45–50, February 2004.

K. Rohlfs and T.L. Wilson. *Tools of Radio Astronomy*. Springer-Verlag Telos, 2nd edition, 1996.

George B. Rybicki and Alan P. Lightman. *Radiative Processes in Astrophysics*. Wiley-VCH, 1985.

D. D. Sokoloff, A. A. Bykov, A. Shukurov, E. M. Berkhuijsen, R. Beck, and A. D. Poezd. Depolarization and Faraday effects in galaxies. *Monthly Notices of the Royal Astronomical Society*, 299:189–206, August 1998. doi: 10.1046/j.1365-8711.1998.01782.x.

M. Tucci, E. Carretti, S. Cecchini, L. Nicastro, R. Fabbri, B. M. Gaensler, J. M. Dickey, and N. M. McClure-Griffiths. Polarization Angular Spectra of Galactic Synchrotron Emission on Arcminute Scales. *The Astrophysical Journal*, 579:607–615, November 2002. doi: 10.1086/342793.

B. Uyaniker, E. Fuerst, W. Reich, P. Reich, and R. Wielebinski. A 1.4 GHz radio continuum and polarization survey at medium Galactic latitudes. I. Observation and reduction technique. *Astronomy and Astrophysics Supplement*, 132:401–411, November 1998. doi: 10.1051/aas:1998449.

Gerrit L. Verschuur. *The Invisible Universe*. Springer, New York, New York, 2nd edition, 2007.

A.G. Willis. Some Synthesis Telescope imaging algorithms to remove non-isoplanatic and other nasty artifacts. *Astronomy and Astrophysics Supplement Series*, 136:603–614, May 1999. doi: 10.1051/aas:1999237.

M. Wolleben, T. L. Landecker, W. Reich, and R. Wielebinski. An absolutely calibrated survey of polarized emission from the northern sky at 1.4 GHz. Observations and data reduction. *Astronomy and Astrophysics*, 448:411–424, March 2006. doi: 10.1051/0004-6361:20053851.

Appendix A

Synchrotron Emission

As previously noted, the main contribution to the observed polarized structures is provided by Faraday rotation of Galactic synchrotron emission. In fact, synchrotron emission dominates emission at all frequencies below 30 GHz for star-forming galaxies such as our own [Condon and Ransom, 2011]. This synchrotron emission, or magnetobrehmsstrahlung, occurs when charged particles such as electrons are accelerated in a magnetic field. By Larmor's formula, acceleration of a charged particle will produce electromagnetic radiation. In the case of synchrotron radiation, the charged particles are relativistic electrons that undergo a uniform circular motion with a constant orbital velocity, resulting in a helical path around the magnetic field lines.

Applying the relativistic corrections to the gyration frequency expected from such electrons gives a frequency in Gaussian units of

$$\omega_B = \frac{eB}{\gamma m_e c}. \tag{A.1}$$

Here γ is the usual Lorentz factor. In order to calculate the power emitted, the Thomson cross section of the electrons for scattering of electromagnetic radiation is determined as

$$\sigma_T = \frac{8\pi}{3} \left(\frac{e^2}{m_e c^2} \right)^2. \tag{A.2}$$

Finally, the effects of the magnetic field are applied as a magnetic energy density $U_B = \frac{B^2}{8\pi}$, giving an emitted power per electron from Larmor's formula of

$$P = 2\sigma_T \beta^2 \gamma^2 c U_B \sin^2 \alpha. \tag{A.3}$$

Here $\beta = \frac{v}{c}$, and α is the pitch angle between the direction of motion of the electron and the direction of the magnetic field. By averaging over a large number of electrons with varying pitch angles but identical velocities the average power can be determined:

$$\langle P \rangle = \frac{4}{3} \sigma_T \beta^2 \gamma^2 c U_B. \tag{A.4}$$

This emitted power is much greater than classically expected from a gyrating electron; it is the relativistic corrections that allow synchrotron emission to be the dominant process at our frequencies of interest [Rybicki and Lightman, 1985].

Aside from the overall power emitted by synchrotron radiation, the dependence of this power on frequency is worth considering. The radiation emitted from such a gyration effect is radiated in the instantaneous direction of motion of the emitting electron. Due to the helical path of the electrons, the aggregate emission is strongly beamed in a cone of emission with an opening angle identical to the pitch angle and its axis pointed along the magnetic field. Relativistic effects cause this cone of emission to narrow as the velocity approaches the speed of light; the emission cone opening is effectively dictated by the electron energies. Furthermore, the emitted synchrotron radiation is only detectable when the emission cone aligns with the observational beam, which occurs very briefly but periodically [Rohlfs and Wilson, 1996].

Each synchrotron pulse is extremely narrow compared to the time between pulses, with a typical pulse duration on the order of 10^{-10} seconds and inter-pulse spacings on the order of 10^3 seconds. The Fourier transform of the pulse train gives a broad spectrum - the observed power spectrum of the emission; this transform consists of a series of peaks so closely spaced in the frequency domain that they appear essentially continuous. Furthermore, as noted in Condon and Ransom [2011], any fluctuations in the electron energy or magnetic field strength causes frequency shifts in the observed spectrum larger than the separations between these closely spaced peaks. The emission from a single electron appears nearly continuous. Applying a cosmic-ray electron energy distribution as observed in our galaxy smears out the spectrum and predicts an accurate measure of the slope of the synchrotron emission in the frequency domain. As calculated in Condon and Ransom [2011], the emission coefficient within our galaxy, ϵ_ν, is

$$\epsilon_\nu \propto B^{1.7} \nu^{0.7}. \tag{A.5}$$

Of primary importance here is the negative spectral index of 0.7 that determines the shape of the radio spectrum below 30 GHz. It should also be noted that the spectrum at frequencies below 1 GHz can be flattened considerably by free-free absorption, though this effect is unimportant at the frequencies considered in this thesis. With a spectral index of 0.7 the ~ 28 MHz spread in centre frequencies for the bands of the Synthesis Telescope (discussed in Section 1.2.3) amounts to a difference of $\sim 4\%$ in amplitude scales.

Synchrotron emission also has an intrinsic polarization due to the alignment of the spiraling electrons. The radiation from a single charge is elliptically polarized, but a distribution of charges will cancel out this elliptical component, leaving the radiation as partially linearly polarized perpendicular to the spiral direction. Comparing the powers emitted parallel and perpendicular to the magnetic field (components of $\langle P \rangle$ above) the maximum fraction of polarization is determined to be between 70 and 75 %. The variation in fractional polarization is due to the slight uncertainty in the power law distribution of electron energies [Rybicki and Lightman, 1985]. As discussed in Section 1.2, the observed polarization fractions are closer to 10%, but this may be due to significant depolarization effects.

Appendix B

Polarization

From Maxwell's equations of electromagnetism we determine that any electromagnetic radiation consists of transverse waves of oscillating electric and magnetic fields. In free space the wave equation for the propagation of the electric field is

$$\nabla^2 \varepsilon = \frac{1}{c^2} \frac{\partial^2 \varepsilon}{\partial t^2}. \tag{B.1}$$

The magnetic field obeys a similar equation, but is found perpendicular to the electric field with the cross product of the two fields determining the direction of propagation of the wave. The electric field is considered here as it is chosen by convention to represent the polarization of the wave. At a significant distance from the source of the radiation the wavefronts are effectively plane-parallel, and a general solution of the wave equation for the electric field takes the following form:

$$\varepsilon(z, t) = (\hat{\mathbf{x}} \varepsilon_x + \hat{\mathbf{y}} \varepsilon_y) \exp[\mathrm{i} 2\pi(\nu t - kz)]. \tag{B.2}$$

In this solution the electric field has an inverse wavelength of $k = 1/\lambda$ and a frequency of ν. The direction of wave propagation is z, and the preceding multiplicative factor expresses the wave amplitude in terms of separate complex amplitudes ε_x and ε_y [Burke, 2010].

The polarization of the wave is thus described by the relative amplitudes of ε_x and ε_y and their relative phase $\delta\phi = \phi_1 - \phi_2$. In this formulation the x and y axes specify a plane that lies perpendicular to the direction of propagation. If the orientation of the electric field remains constant as the wave propagates, then the wave is said to be linearly polarized. If instead the amplitudes are equal but the phases of ε_x and ε_y differ by 90 degrees the wave is circularly polarized, and the combined electric wave vector rotates in the x,y plane. These are the two limiting cases of the general result in which the projection of ε on the x,y plane describes an ellipse in time - elliptical polarization. The wave vector may rotate in either direction, so right-hand elliptical polarization is defined as the vector rotating clockwise when viewed along the direction of propagation; left-hand polarization is the counter-clockwise case [Burke, 2010].

In general the axes of the ellipse need not be aligned with the observational x and y axes, being rotated instead by some angle χ. For this reason the electric field vector may also be described by separating the single amplitude of ε_0 into ε_a and ε_b, which represent the electric field vector components along the major and minor axes of the ellipse respectively:

$$\varepsilon_a = \varepsilon_0 \cos\beta \; ; \quad \varepsilon_b = -\varepsilon_0 \sin\beta. \tag{B.3}$$

The major and minor axes of the ellipse are separated by $\pm\pi/2$, and the parameter β describes the classification of the polarization. For $\beta = 0$ the light is plane-polarized, and for $\beta = \pm\pi/4$ the light is circularly polarized. Thus for the plane waves considered here the polarization is fully specified by the parameter β, the orientation angle of the ellipse χ, and the total amplitude ε_0 [Kraus, 1986].

B.1 Stokes Parameters

The polarization state of an electromagnetic wave can be fully and succinctly represented by the Stokes parameters I, Q, U, and V as defined by George Gabriel Stokes in 1852 [Burke, 2010]. In terms of the elliptical parameters defined at the end of Section B, the Stokes parameters for a monochromatic polarized wave are:

$$I \equiv \varepsilon_0^2, Q \quad \equiv \varepsilon_0^2 \cos(2\beta)\cos(2\chi), U \equiv \varepsilon_0^2 \cos(2\beta)\sin(2\chi), V \quad \equiv \varepsilon_0^2 \sin(2\beta)$$

The Stokes parameters are a particularly useful characterization of the polarization as they are directly related to observable powers. Stokes I is proportional to the total energy flux; Stokes Q and U are determined from LHCP and RHCP power detection; Stokes V is not determined in the current dataset. For Stokes V equal to zero the polarization is entirely linear; conversely, for $V/\varepsilon_0^2 = +1$ the polarization is entirely (right-hand) circular. For fully polarized waves Stokes I is related directly to the polarized Stokes parameters:

$$I^2 = Q^2 + U^2 + V^2 \tag{B.4}$$

As the radiation field is described by the three parameters ε_0, β, and χ, the four Stokes parameters completely describe the radiation field. In the case of completely unpolarized radiation I is the specific intensity of the radiation, with Q, U, and V all zero, and B.4 no longer applies. Instead, a degree of polarization PI can be defined as the ratio of the quadrature sum

of the polarization parameters Q, U, V and the specific intensity:

$$PI = \frac{(Q^2 + U^2 + V^2)^{1/2}}{I}.$$ (B.5)

The observations analyzed in this thesis are made in two orthogonal polarizations, which allows us to specify Q and U, while leaving Stokes V unknown. In this case the degree of linear polarization can be determined by the above equation with V = 0. For the present data the expected degree of linear polarization is less than 70 %, the theoretical maximum for synchrotron emission [Sokoloff et al., 1998].

Finally, the polarization angle χ can be determined by rearranging Stokes Q and U:

$$\chi = \frac{1}{2} \arctan \left(\frac{U}{Q} \right).$$ (B.6)

It should also be noted that in reality we do not measure single monochromatic waves, but rather a time-average of many superpositions over some finite bandwidth of the receiver, so the above equations should be considered as time- and bandwidth-averaged values determined from the power measurements of the telescope receiver [Burke, 2010].

B.2   Faraday Rotation

Radiation emitted within the Galaxy does not travel to the telescopes on Earth unhindered or unaffected by the media it traverses. Interactions with the interstellar medium may cause the radiation to be absorbed, scattered, or otherwise fundamentally altered. Of importance for the observations presented in this thesis, and generally for any radio polarization studies, are the effects of Faraday rotation. As an electromagnetic wave passes through a plasma the electrons in the plasma respond to the changing electric field by oscillating and re-radiating at the wave frequency, giving the plasma a certain refractive index [Burke, 2010]. The presence of a static magnetic field forces the moving electrons into curved paths reminiscent of the synchrotron mechanism responsible for the original emission. However, the response of the polarized wave components to this refractive index differs depending on the direction of polarization. Considering the linearly polarized emission to be a combination of left and right circular polarizations, the effect causes the circular polarizations to move at different speeds through the medium. This relative phase shift of the circular polarizations amounts to a rotation of the linear polarization [Burke, 2010].

In essence the plasma through which the electromagnetic wave is propagating is birefringent, with a refractive index for the two circular polarizations of

$$n^2 = 1 - \frac{\omega_p^2}{\omega(\omega \pm \omega_B)}.$$ (B.7)

Here the gyration frequency is given by the nonrelativistic form:

$$\omega_B = \frac{eB}{m_e c}.$$ (B.8)

As the electrons are required to gyrate perpendicular to the wave direction in order to have a significant effect, the Faraday rotation effect is dominated by the component of the magnetic field aligned with the direction of wave propagation. In the radio regime, the angle of total rotation along a ray path is given by θ_R:

$$\theta_R = RM\lambda^2$$ (B.9)

where RM is the rotation measure of the ray path in rad m^{-2}. For distances in parsecs, density in cm^{-3}, and magnetic field in microgauss, this rotation measure is

$$RM = 0.81 \int BN \cos\theta \, dl.$$ (B.10)

In studies of the rotation measure along various sight-lines the value of RM can be determined from observations at multiple frequencies by comparing the angles of rotation. As this thesis deals with single-frequency measurements alone, no calculations of rotation measure are made. It should be noted that a rough analysis of rotation measure is possible due to the four frequency bands utilized in the synthesis telescope, but the sensitivity required is lacking. Nonetheless, Faraday rotation causes much of the small-scale variation seen in the polarization angle [Landecker et al., 2000]. Faraday rotation may also be responsible for significant depolarization as discussed in Section B.3.

B.3 Depolarization Mechanisms

As this thesis and the observations considered herein are polarization studies, any effects that can cause erroneous polarization features need to be determined in detail. The various effects that can cause depolarization or a loss of polarization in the measurements are discussed here.

An important source of depolarization is differential Faraday rotation or depth depolarization. Faraday rotation in isolation does not cause depolarization since it merely changes the polarization angle. However, if a medium contains both thermal and relativistic electrons and some semi-ordered magnetic field then the synchrotron emission at varying depths in the medium will undergo different amounts of Faraday rotation. With a significantly broad distribution of Faraday rotations these components can begin to cancel and effectively reduce the polarized intensity. This results in a reduced polarization fraction of the observed emission dependent on the rotation measure along the line of sight [Sokoloff et al., 1998]. In such circumstances the observed polarized intensity is given by

$$I = I_0 \left| \frac{sin(2RM\lambda^2)}{2RM\lambda^2} \right| \tag{B.11}$$

[Haverkorn et al., 2004]. Depth depolarization also contains a contribution from variations of the emitted polarization angles along a line of sight; that is, the polarization of the synchrotron emission along the line of sight may vary, and the superposition of these vectors may lead to partial cancellation.

The other significant source of depolarization occurs across the beam of the receiver, and is termed beam depolarization. This depolarization is simply the result of vector addition of differing polarizations for different lines of sight within a single telescope beam, and has no dependence on wavelength. This effect strongly contributes to depolarization canals in polarized intensity maps [Haverkorn et al., 2004]. Such canals appear as filamentary structure of one beam width with lower polarized intensity than the surroundings. The polarization angle also changes by 90° across each canal. Haverkorn et al. [2004] argue that these canals exist between two regions which have a polarization angle difference of $\delta\phi = (n + 1/2)180°$ $(n = 0, 1, 2, ...)$, which causes the vector addition across the beam to return almost zero polarized intensity. If this rapid transition in polarization angle occurs within a beam then the resulting region of depolarization will clearly have a width of a single beam.

The analysis by Landecker et al. [2010] of the CGPS maps used in this thesis indicates that along directions close to a galactic longitude of 85° there is significant Faraday rotation and depolarization effects. The ordered component of the local magnetic field is in the direction of $\ell = 85°$, allowing for greater Faraday rotation. Shifting the line of sight closer to the anticenter of the Galaxy shows decreased Faraday rotation as the line of sight becomes perpendicular to the regular component of the magnetic field. A strong decrease in depolarization is seen with an increase in polarization fraction.

The synchrotron emission in the direction of the anticenter also decreases as evidenced by the reduction in total intensity.

Depolarization is also strong in nearby HII regions where Faraday rotation is produced by the abundance of free electrons; this effect is seen in the polarization images as a sudden drop in polarized intensity at the edges of HII regions. (HII regions can be viewed in total intensity or Hα maps.) The HII regions depolarize more distant emission, and may have little intrinsic synchrotron emission on the near side to our observations. Less drastic depolarization occurs when distant emission from the Perseus Arm passes through HII regions in the closer Local Arm. The polarized emission in these directions is fairly smooth, probably due to synchrotron emission on the near side of the HII regions which then undergoes little further Faraday rotation. Further discussion of specific depolarization regions can be found in Wolleben et al. [2006], Kothes and Landecker [2004], Landecker et al. [2010].

There exists a distance beyond which we are unable to measure polarization due to the combined effects of differential Faraday rotation and beam depolarization. Beyond this distance all polarized emission has been effectively depolarized, thus it is termed the polarization horizon. The exact distance depends on the frequency of the measurements, beamwidth, and the direction of the line of sight. Between $\ell \approx 66°$ and $\ell \approx 100°$ the observed polarization features are predominantly local - within 2 kpc [Kothes and Landecker, 2004]; at greater longitudes the features are a combination of large, smooth local features and seemingly random small-scale structure from the Perseus arm. Near the galactic anticenter the polarization horizon is beyond the Perseus arm, and possibly beyond the extent of the Galaxy [Landecker et al., 2010].